

ARTICLE

Modified plastic damage model for steel fiber reinforced concrete

Tung T. Tran¹ | Thong M. Pham²  | Duong T. Tran³  | Ngoc San Ha⁴ | Hong Hao^{3,5}

¹Arup Perth, Perth, Western Australia, Australia

²UniSA STEM, University of South Australia, Mawson Lakes, South Australia, Australia

³Center for Infrastructural Monitoring and Protection, School of Civil and Mechanical Engineering, Curtin University, Bentley, Western Australia, Australia

⁴School of Engineering, RMIT University, Melbourne, Victoria, Australia

⁵Guangdong Provincial Key Laboratory of Earthquake Engineering and Applied Technology, Earthquake Engineering Research and Test Center, Guangzhou University, Guangzhou, China

Correspondence

Hong Hao, Guangdong Provincial Key Laboratory of Earthquake Engineering and Applied Technology, Earthquake Engineering Research and Test Center, Guangzhou University, China; and Center for Infrastructural Monitoring and Protection, School of Civil and Mechanical Engineering, Curtin University, Kent Street, Bentley, WA 6102, Australia.
Email: hong.hao@curtin.edu.au

Thong M. Pham, UniSA STEM, University of South Australia, Mawson Lakes, South Australia, Australia.
Email: thong.pham@unisa.edu.au

Funding information

Australian Research Council Laureate Fellowships, Grant/Award Number: FL180100196

Abstract

Steel fiber reinforced concrete (SFRC) structures have been widely adopted and attracted great research attention due to their excellent performance in resisting tension and flexure bending. However, the existing analytical and numerical analyses of SFRC structures rely mainly on the experimental data of material tests, thereby being suitable for a case-by-case basis. This is due to the lack of a general and reliable constitutive material model for SFRC, which analytically considers the fiber-dependent parameters such as fiber geometry, fiber stiffness, and interface properties of fibers and concrete matrix. This study presents an approach to modify the concrete plastic damage model to represent the SFRC material constitutive relations for simulating the structural behavior of SFRC. In this approach, the general procedure to integrate the bridging effect of fibers through the pull-out mechanism into the constitutive relation of SFRC was proposed. The comparison between the numerical and experimental results was conducted to verify the reliability of the proposed model. The results demonstrated the proposed model could well represent the material performance of SFRC and the numerical simulations could capture reasonably the effect of the volume fraction, geometry, and properties of fibers on the structural response of SFRC.

KEYWORDS

abaqus, concrete damaged plasticity model, constitutive model, fiber reinforced concrete, simulation

1 | INTRODUCTION

Plain concrete is intrinsically brittle and has a low capacity under tension, which can result in premature failure of structures. Therefore, considerable efforts to improve the concrete properties have been made over the recent decades. Among those attempts, the incorporation of fibers into the concrete matrix is one of the effective approaches.¹⁻³ In terms of the material properties, steel fiber reinforced concrete (SFRC) demonstrates superior performance in tension capacity, energy absorption, impact resistance, fracture toughness, and postcracking behavior.⁴⁻⁷ The key feature of SFRC is the ability to transfer the tension stress after the formation of cracks in the mortar, which helps postpone the crack propagation and opening. In terms of structural scale, many previous studies demonstrated that fiber reinforcement significantly enhanced the capacity, ductility, and postpeak behavior of reinforced concrete beams, columns, and beam-column joints.^{8,9} However, most of the research attention is currently focusing on experimental investigation whereas only a few studies paid attention to developing or investigating constitutive material models for SFRC. Therefore, the current procedure for simulating SFRC structures requires many experimental data from material tests for calibration, thereby being applicable on a case-by-case basis.

The available material models of SFRC in the literature have been derived from three primary methods: (1) discrete method, (2) empirical calibration, and (3) continuum-damage based theory. These methods have shown pros and cons when being adopted for developing a constitutive material model. First, the discrete method adopted the concept of separating the fiber phase from the concrete matrix phase, thereby increasing the computational cost significantly.¹⁰⁻¹² Even though the discrete-based models such as lattice models could predict accurately the response of SFRC at the mesoscale level, their complexity and high computational cost impeded them from being deployed in large-scale structures. The second method, which is simpler and more feasible, is to calibrate the material parameters of a plain concrete model based on experimental tests of SFRC.¹³⁻¹⁶ However, this method is mainly based on fitting experimental data, and hence the fiber bridging mechanism cannot be physically captured in the calibrated models, which may lead to a significant error in prediction if those models are employed in other cases. This type of model is based on a case-to-case basis since a calibrated model for a particular concrete with a certain type and volume fraction of fiber may not be applicable for other SFRC. Finally, the available approaches based on the continuum-damage theory exhibited a balance between

computational cost and accuracy. Those models taking into account of essential fiber bridging mechanism are able to reflect the variation in structural performance due to the effect of volume fraction and fiber orientation with a reasonable computational cost.¹⁷⁻¹⁹

From the above reviews, the mechanics-based continuum-damage theory is an effective approach for deriving a constitutive model of SFRC. However, in the literature, the constitutive models derived from this approach are still scarce and have several limitations.^{17,19} Those models provided the fundamental concept at the material level, and they have not been verified for large-scale structural components. In addition, to implement those models, a user-material subroutine suitable for finite element software is usually required, which is not convenient in practice.²⁰ To overcome these difficulties, this study proposes a procedure to modify the concrete damaged plasticity model (CDPM) in ABAQUS. The principal components of CDPM for SFRC including the yield criterion, dilation angle of flow rules, damage evolution, and hardening/softening rules are proposed to capture the crack bridging stress of fibers. The derivation is based on the physical working mechanism of steel fibers.

2 | CONCRETE DAMAGED PLASTICITY MODEL

2.1 | Overview

The nonlinearity of concrete behavior can be characterized by two distinguished mechanical processes: (1) damage evolution, which is caused mainly by the microcrack coalescence and macroscopic crack growth; and (2) irreversible deformation such as the inelastic volumetric expansion. The use of continuum damage mechanics can simulate the damage process in concrete, thereby capturing the degradation of stiffness and the softening behavior.^{21,22} Meanwhile, the theory of plasticity can be successfully applied to capture the inelastic deformation of concrete during the unloading process. Therefore, the constitutive models based on the combination of both theories of damage mechanics and plasticity are one of the most effective approaches to simulate the nonlinear behavior of concrete.

In brief, the CDPM, which is first introduced by Lubliner et al.²³ and later modified by Lee and Fenves,²⁴ is presented in this section before modifications presented in the next section. The model adopts the isotropic hardening in a combination with the isotropic damage to achieve simplicity but ensure the necessary accuracy. The key elements of this model including the yield criterion,

flow rule, hardening/softening rule, and function of damage evolution are summarized subsequently.

2.2 | Yield function

The yield function proposed by Lubliner et al.²³ and later modified by Lee and Fenves²⁴ is adopted in CDPM. In the effective stress space, the function is expressed in the following form

$$f(\sigma_1, \sigma_2, \sigma_3) = \frac{1}{1-\alpha} \left(q - 3\alpha p + \left(\frac{\bar{\sigma}_c(\bar{\epsilon}_{pc})}{\bar{\sigma}_t(\bar{\epsilon}_{pt})} (1-\alpha) - (1+\alpha) \right) \langle \bar{\sigma}_{\max} \rangle - \gamma \langle -\bar{\sigma}_{\max} \rangle \right) - \bar{\sigma}_c(\bar{\epsilon}_{pc}) \quad (1)$$

where α and γ are dimensionless constants to be calibrated from material tests; p is the effective hydrostatic pressure; q is the Mises equivalent effective stress; $\bar{\sigma}_{\max}$ is the maximum of principal stress; $\bar{\sigma}_c(\bar{\epsilon}_{pc})$ and $\bar{\sigma}_t(\bar{\epsilon}_{pt})$ are respectively the effective compressive and tension cohesion stress determined by the hardening/softening rule; and $\bar{\epsilon}_{pc}$ and $\bar{\epsilon}_{pt}$ are the equivalent compressive and tension plastic strain, respectively.

The constants α governing the biaxial compressive stress state can be determined based on the ratio between the equivalent biaxial compressive strength f_{bc} and uniaxial compressive strength f'_c by using Equation (2). Meanwhile, the parameter γ governing the triaxial stress state is calculated from Equation (3) where K_c is the ratio of J_2 on the tensile meridian and that on the compressive meridian, respectively. According to experimental evidence of plain concrete, the ratio f_{bc}/f'_c are in the range from 1.10 to 1.16 while K_c is conventionally taken as 2/3 in this study.

$$\alpha = \frac{f_{bc}/f'_c - 1}{2f_{bc}/f'_c - 1} \quad (2)$$

$$\gamma = \frac{3(1-K_c)}{2K_c - 1} \quad (3)$$

2.3 | Flow rule

Due to the significant change in the volumetric strain of concrete material, the nonassociated flow rules are commonly used in the constitutive model of concrete including CDPM. The potential function adopted in this model is the Drucker-Prager hyperbolic function:

$$G = \sqrt{(\epsilon f_{ct} \tan \psi)^2 + q^2} - p \tan \psi \quad (4)$$

where ψ is the dilation angle measured in the p - q plane at high confining pressure; f_{ct} is the uniaxial tensile stress at failure; and ϵ is the parameter, referred as the eccentricity, that defines the rate at which the function approaches the asymptote. This flow potential, which is continuous and smooth, ensures that the flow direction to be uniquely determined.

2.4 | Hardening and softening rules

In the CDPM, isotropic hardening/softening rules are adopted and the function with controlling parameters are defined as the equivalent plastic strain. Due to the significant difference in the compression and tension behaviors, the hardening/softening rules of concrete are defined by two different functions $\bar{\sigma}_c(\bar{\epsilon}_{pc})$ and $\bar{\sigma}_t(\bar{\epsilon}_{pt})$ as expressed in Equation (1). Under the uniaxial stress state, by assuming that the direction of the principal stress σ_1 is the loading direction, the remaining principal stresses σ_2 and σ_3 equal to zero. By substituting the uniaxial condition in Equation (1), the effective compressive and tensile stresses for uniaxial loading is reformulated as follows:

$$\bar{\sigma}_c(\bar{\epsilon}_{pc}) = \sigma_1(\epsilon_{pc}) \text{ if } \sigma_1 < 0 \quad (5)$$

$$\bar{\sigma}_t(\bar{\epsilon}_{pt}) = \sigma_1(\epsilon_{pt}) \text{ if } \sigma_1 > 0 \quad (6)$$

From Equations (5) and (6), the hardening/softening rules of CDPM have to match with the stress versus plastic strain curve of concrete under uniaxial tension and compression loading. In ABAQUS, for convenience, the tabular form of stress versus inelastic strain extracted from uniaxial tests can be used as inputs. Then, the software automatically converts the inelastic strain (ϵ_{inc} for compressive behavior and ϵ_{int} for tension behavior) into the plastic strain based on the following expressions

$$\epsilon_{pc} = \epsilon_{inc} - \frac{d_c}{1-d_c} \frac{\sigma_c}{E_c} \quad (7)$$

$$\varepsilon_{pt} = \varepsilon_{int} - \frac{d_t}{1 - d_t} \frac{\sigma_t}{E_c} \quad (8)$$

where σ_c and σ_t are stress points obtained from the uniaxial compressive and tension tests, respectively; E_c is the elastic modulus of concrete; d_c and d_t are respectively the damage variables in compression and tension determined from damage laws, which are presented in the next section.

2.5 | Damage

The inelastic behavior of a ductile material can be simulated by adopting the plasticity theory where the total strain tensor $[\varepsilon]$ can be decomposed into two parts including the elastic strain tensor $[\varepsilon_e]$ and plastic strain tensor $[\varepsilon_p]$, and then stress state can be determined as follows:

$$[\varepsilon] = [\varepsilon_e] + [\varepsilon_p] \quad (9)$$

$$[\sigma] = [D]_e([\varepsilon] - [\varepsilon_p]) \quad (10)$$

where $[\sigma]$ is the stress tensor and $[D]_e$ is the initial stiffness tensor. Figure 1 illustrates the loading and unloading response of a material described by the plasticity theory. It can be seen that the initial stiffness of the material remains unchanged under the unloading condition, thereby the inelastic strain ε_{in} equaling to the plastic strain ε_p (see Figure 1). However, the degradation of the unloading stiffness of concrete material always occurs

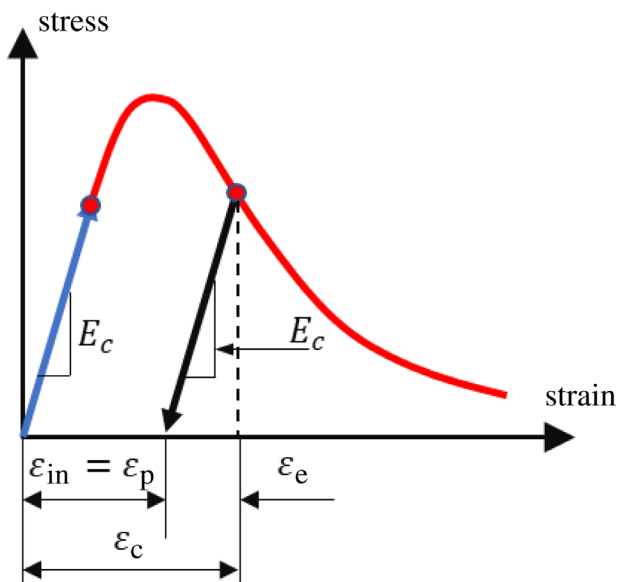


FIGURE 1 Loading and unloading responses of the elastoplastic model.

due to damage (see Figure 2). This leads to the fact that the inelastic behavior of concrete material cannot be entirely reflected by the plasticity theory. Hence, CDPM adopts a scalar variable d , $0 \leq d \leq 1$, to simulate the progressive material damage of concrete as

$$[\sigma] = (1 - d)[D]_e([\varepsilon] - [\varepsilon_p]) \quad (11)$$

Under the uniaxial monotonic loading conditions, variable d can be characterized by two damage variables d_c and d_t that respectively represent damage of concrete in compression and tension. Therefore, Equation (11) can be expressed in the scalar form for the uniaxial loading condition as follows

$$\sigma_c = (1 - d_c)E_c(\varepsilon_c - \varepsilon_{pc}) \quad (12)$$

$$\sigma_t = (1 - d_t)E_c(\varepsilon_t - \varepsilon_{pt}) \quad (13)$$

where E_c is the elastic modulus of concrete; ε_c and ε_{pc} are respectively the total strain and plastic strain in compression; and ε_t and ε_{pt} are the total strain and plastic strain in tension respectively.

3 | PROPOSED MODIFICATION FOR SFRC

3.1 | General

The presence of macro steel fibers improves the mechanical characteristics of concrete material through the

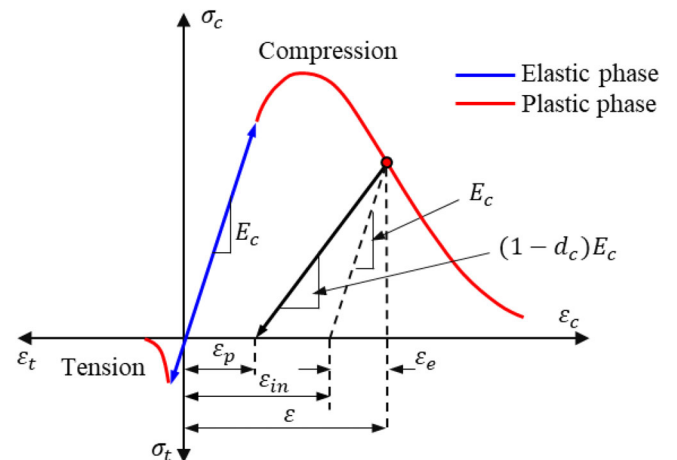


FIGURE 2 Loading and unloading responses of damage plastic model of concrete.

FIGURE 3 Uniaxial tension curves including σ_c versus ϵ_c and σ_c versus w (crack opening displacement) of plain and fiber reinforced concrete.

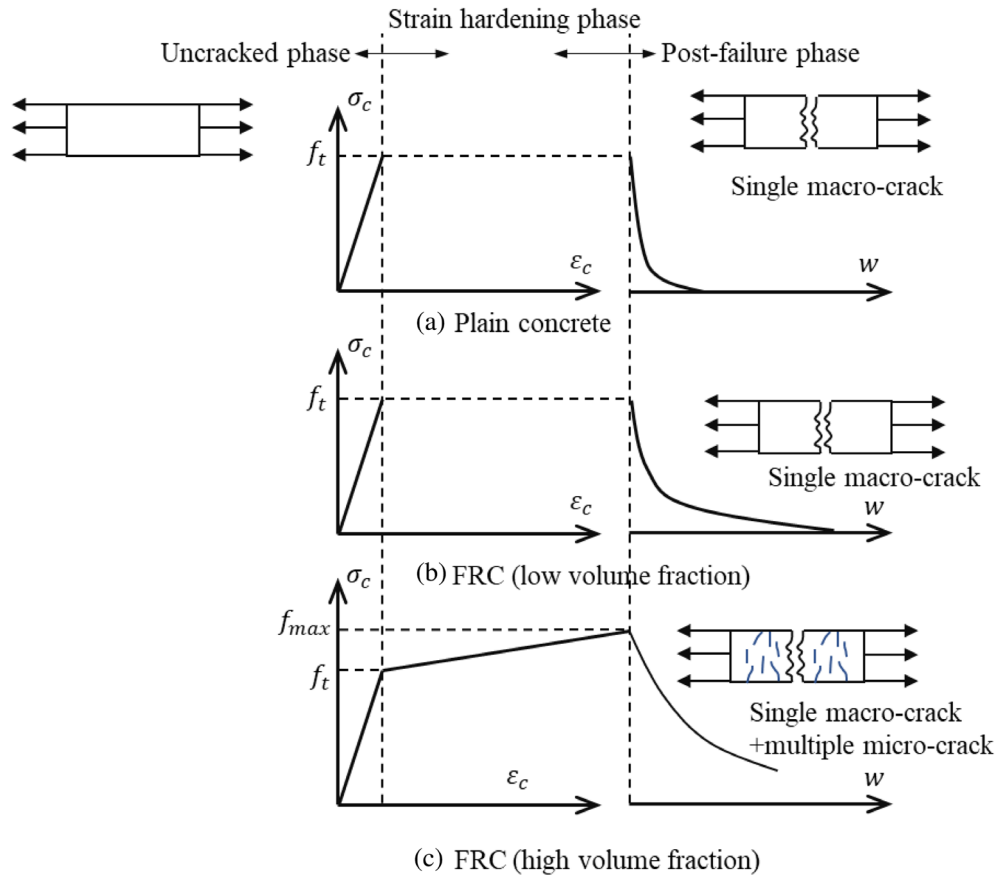
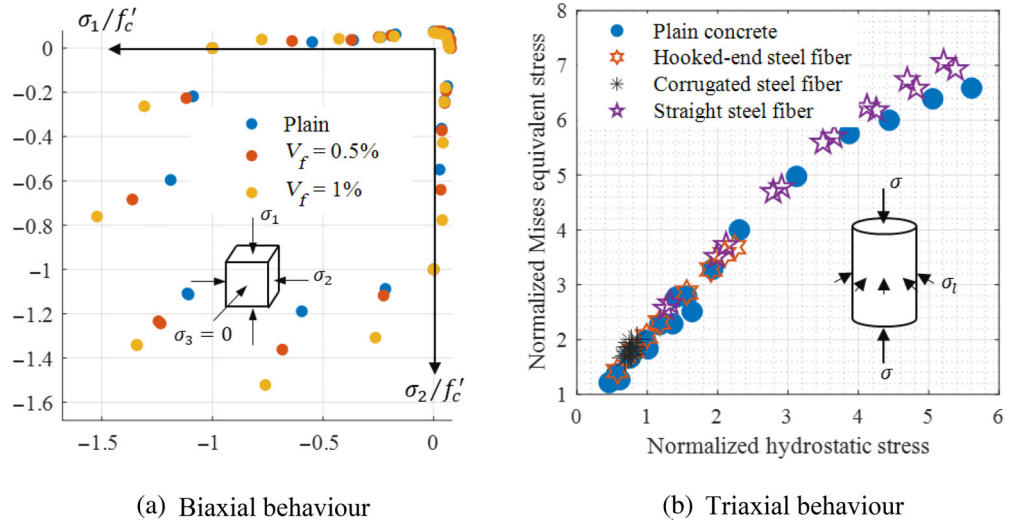


FIGURE 4 The experimental data of plain and fiber reinforced concrete under compressive biaxial tests²⁹ and triaxial tests.^{30–33} (a) Biaxial behavior and (b) triaxial behavior.



bridging effect at cracks. In terms of the tension behavior, the postpeak behavior of SFRC is significantly better than that of plain concrete (see Figure 3). When a high fiber volume fraction is used, SFRC can attain the strain hardening behavior after the formation of first crack (Figure 3c). This observation demonstrates that the tension behavior of SFRC is significantly different from plain concrete. Accordingly, the aspects of CDPM related to the tension response including the tension softening rules

and tension damage rules are modified to consider the bridging effect of fibers.

In terms of the compressive behavior, the previous studies indicated that the bridging effect of fiber at cracks can result in the slight passive confining stress in out-of-plane direction.^{25–28} However, that influence is only effective in improving the biaxial strength of SFRC^{26,27,29} (as seen in Figure 4a) while the uniaxial and triaxial strength of SFRC seems to be not much different from

the plain concrete^{30–33} (see Figure 4b). Furthermore, the confining stress yields smaller plastic volumetric strain, thereby leading to a reduction of the dilation characteristics (i.e., dilation angle) of SFRC. Therefore, the confining effect of fiber reinforcement is necessary to be considered in the compressive behavior of SFRC. Based on the above discussion, the primary modifications of CDPM for SFRC are presented as follows:

- Since the confining effect of fibers on the compressive behavior of SFRC is considered, the ratio f_{bc}'/f_c' in Equation (2) and the dilation angle ψ in Equation (4) are modified. Meanwhile, the constant governing the triaxial state of yield surface K_c in Equation (3) remains similar to plain concrete.
- The available empirical model for SFRC under the compressive uniaxial loading is adopted to calculate the compressive hardening/softening rules and the compressive damage law.
- The crack bridging effect of fibers into the tension hardening/softening rules and the tension damage law for SFRC is analytically considered and the corresponding derivations are made.

3.2 | Yield function

As mentioned in Section 2.2, the yield function of CDPM is governed by two constants α and γ . The first constant governs the yield surface at the compressive biaxial failure state while the second one controls the shape of the deviatoric plane of the yield surface at the compressive triaxial failure state. As discussed in Section 2.2, the experimental findings in the literature indicated that triaxial failure state of SFRC was quite similar to plain concrete. Thus, the effect of fiber reinforcement on constant γ is negligible. Meanwhile, the compressive equibiaxial strength of SFRC has been consistently higher than that of plain concrete, which indicates that the fiber presence has a significant influence on the biaxial failure state of concrete material. Therefore, constant α is affected by the incorporation of fibers and it is modified for SFRC as described in the following section.

3.2.1 | Constants α and ratio f_{bc}'/f_c'

Under the biaxial compression, the failure of plain concrete is caused by the tensile splitting cracks parallel to the unloaded face. Before cracking, the presence of steel fibers has a negligible influence on the stress–strain response of SFRC.^{26,27} However, after cracking, the

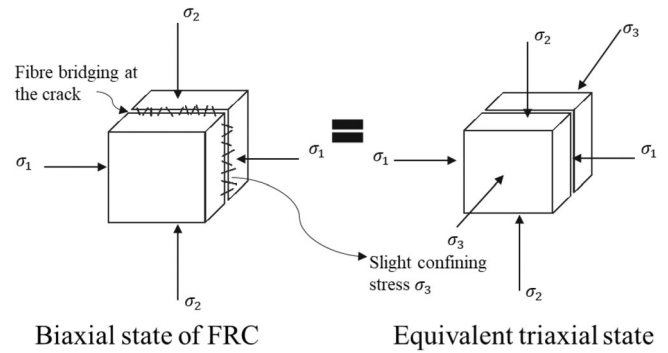


FIGURE 5 Equivalent triaxial state to determine the biaxial compressive strength of steel fiber reinforced concrete.

inclusion of fibers reduces the lateral strain in the unloaded direction considerably, thereby inducing confining pressure. According to the test data, previous investigations demonstrated that the increase in biaxial compressive strength of fiber concrete could be attributed to this confining pressure of fibers.^{26,27,29} In addition, the inelastic behavior of SFRC under biaxial compression can be considered to be similar to that of plain concrete under triaxial state of stress.²⁵ Hence, in the present study, the inclusion of fibers in the concrete is treated as analogous to applying a confining pressure in the direction of σ_3 . That is, the strength envelope for SFRC under biaxial compression (σ_1, σ_2) can be regarded as equivalent to the failure envelope for an analogous plain concrete under triaxial compression ($\sigma_1, \sigma_2, \sigma_3$), where σ_3 is the confining pressure (see Figure 5). The value of the confining pressure in the σ_3 direction is assumed to be equal to σ_{tu} where σ_{tu} is the residual postcracking tensile strength as proposed by Lim et al.³⁴ Although there is a need to incorporate the fiber pull-out characteristics, this modeling can be considered satisfactory, in the case that most of the available models for plain concrete also attempt to model the failure envelopes using only stress variables.²⁷

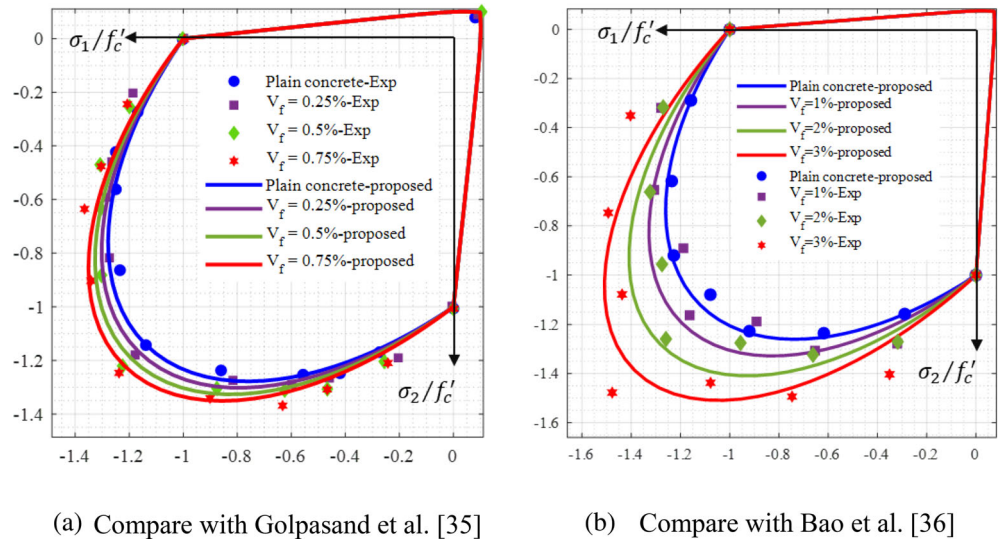
Based on the above discussions and assumptions, the equation for equibiaxial state of SFRC is presented as follows

$$f(0, f_{bc}^{\text{fiber}}, f_{bc}^{\text{fiber}}) = f(\sigma_{tu}, f_{bc}, f_{bc}) \quad (14)$$

where f is the yield function expressed in Equation (1). By solving the equation, the ratio of $f_{bc}^{\text{fiber}}/f_c^{\text{fiber}}$, and α^{fiber} is obtained by Equations (15) and (16) as:

$$\frac{f_{bc}^{\text{fiber}}}{f_c^{\text{fiber}}} = \frac{\sigma_{tu}}{f_c'} \frac{1 + 2\alpha + \gamma}{1 - 2\alpha} + \frac{f_{bc}}{f_c'} \quad (15)$$

FIGURE 6 Biaxial strength envelope for steel fiber reinforced concrete. (a) Compare with Golpasand et al.³⁵ and (b) compare with Bao et al.³⁶



$$\alpha^{\text{fiber}} = \frac{(f_{bc}^{\text{fiber}}/f_c^{\text{fiber}}) - 1}{(2f_{bc}^{\text{fiber}}/f_c^{\text{fiber}}) - 1} \quad (16)$$

where f_c^{fiber} is the uniaxial compressive strength of SFRC and f'_c is that of plain concrete. From the above equations, it can be seen that the parameter α^{fiber} depends on σ_{tu} , which can be generally derived from the pull-out mechanism³⁴

$$\sigma_{tu} = 2\eta_1\eta_0 \frac{V_f L_f \tau_u}{d_f} \quad (17)$$

where η_0 is the orientation factor taken as 0.405, V_f is the volume fraction of fibers, L_f and d_f are respectively the length and diameter of a fiber, τ_u is the ultimate bond strength of steel fibers and concrete matrix taken as $0.4\sqrt{f'_c}$, and η_1 is the length efficiency factor taken as 0.5 when $L_f \leq L_c$ and $1 - L_c/(2L_f)$ when $L_f > L_c$. L_c denotes the length required to develop the ultimate fiber stress τ_u , that is, $L_c = 0.5\sigma_{fu}d_f/\tau_u$.³⁴ By adopting the α^{fiber} in the yield function, the total envelop of biaxial state in case of SFRC was obtained and compared to the experimental data from the previous studies of Golpasand et al.³⁵ and Bao et al.³⁶ (as shown in Figure 6). It can be seen from the figure, the biaxial failure of SFRC is well predicted for specimens adopting the volume fraction of fibers from 0% to 1%. However, with the increase in the volume fraction of fibers, the proposed model tends to underestimate the biaxial strength of SFRC. This can be attributed to the conservative assumption of the equivalency between fibers confining stress and residual stress of SFRC determined in Equation (17). It should be noted that Equation (17) was derived for SFRC with the softening postcrack behavior, that is, volume fraction of fibers ranging from 0% to 2%.³⁴ With the higher volume

fraction, the postcrack response of SFRC show hardening behavior, thus the confining stress of fibers might be higher than the value estimated from Equation (17). Although further studies can be conducted to achieve the more accurate modeling of case with high-volume fractions, this modeling can be considered satisfactory for engineering practice where the practical maximum fiber volume fraction is limited to about 1%–2%. Figure 7 shows the variation of triaxial failure of SFRC by adopting the modified parameter α^{fiber} . Due to the increase of the fiber volume fraction, the triaxial strength of SFRC increases slightly and the proposed model can capture this phenomenon. However, the yield function proposed by Lubliner et al.²³ in Equation (1) is not suitable for representing the failure of concrete under high hydrostatic pressure (higher than five times uniaxial compressive strength). Therefore, discrepancy between the estimated values and test data from hydrostatic pressures over 120 MPa can be observed from the figure. Modeling the behavior of concrete under large hydrostatic pressures is out of the scope of the proposed model.

3.3 | Flow rule

According to the definition of potential flow function G shown in Equation (4), the dilation angle is the vital parameter that governs the flow rule. In order to refine it more conveniently, two assumptions are adopted, that is, (a) the plastic flow angle is not associated with Lode angle, and (b) the flow direction of the total plastic strain is always identical to that of plastic strain increment. Hence, according to Papanikolaou and Kappos,³⁷ the following geometrical relationship can be obtained:

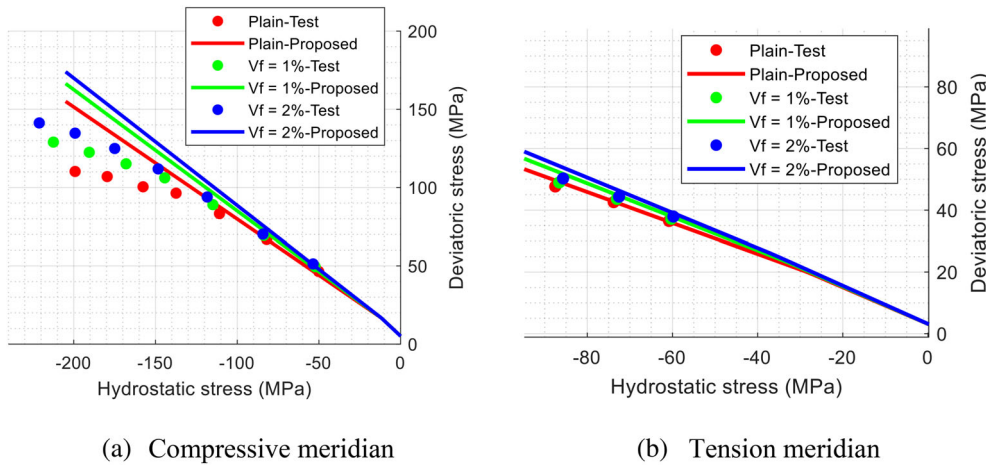


FIGURE 7 Failure state of triaxial compressive loading for steel fiber reinforced concrete (comparison with Jenn-Chuan Chern and Hong.³⁰) (a) Compressive meridian and (b) tension meridian.

$$\theta = -\frac{dp}{dq} = -\frac{dp}{dG} \frac{dG}{dq} = -\frac{q}{\tan\psi \sqrt{(\epsilon_{ct} \tan\psi)^2 + q^2}} \quad (18)$$

It should be noted that the linear potential function, $G = q - p \tan\psi - C$, is equivalent to the Drucker-Prager hyperbolic function in Equation (4) when the hydrostatic pressure p is compressive. Hence, for simplicity, the linear potential function is used for determining the dilation angle. By substituting the linear form of function G into flow rule $\dot{\epsilon}^p = \dot{\lambda} \frac{\partial G}{\partial \sigma}$, the dilation angle can be calculated as follows:

$$d\epsilon_1^p = \left(\frac{1}{3} \tan(\psi) + \frac{2\sigma_1 - \sigma_2 - \sigma_3}{2q} \right) d\lambda \quad (19)$$

$$d\epsilon_2^p = \left(\frac{1}{3} \tan(\psi) + \frac{2\sigma_2 - \sigma_1 - \sigma_3}{2q} \right) d\lambda \quad (20)$$

$$d\epsilon_3^p = \left(\frac{1}{3} \tan(\psi) + \frac{2\sigma_3 - \sigma_2 - \sigma_1}{2q} \right) d\lambda \quad (21)$$

$$d\epsilon_v^p = d\epsilon_1^p + d\epsilon_2^p + d\epsilon_3^p = \tan(\psi) d\lambda \quad (22)$$

$$d\epsilon^p = \sqrt{\frac{1}{2} \left((d\epsilon_1^p - d\epsilon_2^p)^2 + (d\epsilon_2^p - d\epsilon_3^p)^2 + (d\epsilon_3^p - d\epsilon_1^p)^2 \right)} = \frac{3}{2} d\lambda \quad (23)$$

$$\frac{d\epsilon^p}{d\epsilon_v^p} = \frac{\epsilon^p}{\epsilon_v^p} = -\frac{3}{2 \tan(\psi)} \quad (24)$$

Physically, the incorporation of fiber leads to the equivalent confinement on the concrete matrix as mentioned in the previous section, therefore the dilation angle of SFRC may be reduced due to a smaller plastic volumetric deformation. The similar phenomenon has

also been reported in previous investigations on the FRP confined concrete.^{38–41} The dilation rate of concrete reduces due to the presence of passive confining stress of FRP. With the purpose to reflect the function of fibers reasonably, it is assumed that the dilation angle of SFRC is equivalent to that of confined concrete with the fiber confined stress equaling to the residual post cracking stress, σ_{tu} . This assumption is deemed reasonable since the post cracking stress of SFRC postpones the splitting crack development, thereby reduces the rate of plastic volumetric expansion. The function of dilation rate of normal concrete under confined stress σ_{tu} is³⁸

$$\beta = \frac{-2}{a \left(\frac{\sigma_{tu}}{f_c} \right)^b + 1} - 0.5 = \frac{d\epsilon_1^p}{d\epsilon_3^p} \quad (25)$$

where $a = 65e^{-0.015f_c}$; $b = 1.5 - e^{-0.02f_c}$. By substituting the dilation rate into Equation (24), the dilation angle of FRC can be expressed as follows

$$\psi^F = \psi(\sigma_{tu}) = \frac{1}{2} \frac{2\beta + 1}{\beta - 1} \quad (26)$$

The predictions are plotted against the test results extracted from the previous study in Figure 8, from which there are scatter results even though the relationship between the dilation angle and fiber content is quite clear. This means that the actual fiber confining stress might not totally equal the residual post cracking stress. Future studies can be conducted to improve the model by add one calibration factor to the residual stress for matching the experimental test. In this study, due to the lack of test data of dilation rate for SFRC, the fiber confining stress is still assumed to be σ_{tu} as also adopted by the previous study.²⁷

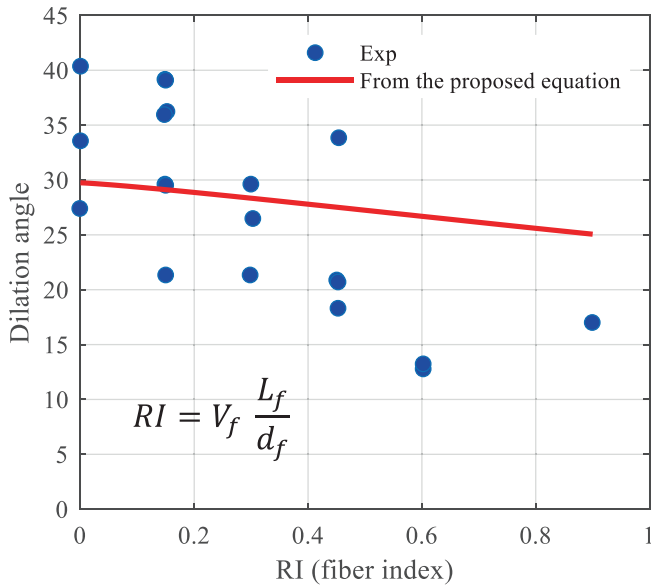


FIGURE 8 Dilation angle of steel fiber reinforced concrete (comparison with Chi et al.⁴²).

3.4 | Hardening and softening rules

3.4.1 | Compressive behavior

Experimental results from the previous study¹⁷ indicated that fiber reinforcement leads to the advantageous effects on the uniaxial compression of concrete specimens such as:

- The compressive strength slightly increases with the fiber volume fraction.
- The strain at peak stress increases with the fiber volume fraction.
- The slope of the postpeak stress–strain relation decreases with the increase of the fiber volume fraction and aspect ratio of fibers.

The compressive hardening/softening function in the previous study¹⁷ is employed in this study. This function, providing a smooth transition from pre to post peak response, is expressed as follows:

$$\frac{\sigma_c}{f_c^{\text{fiber}}} = Y(\eta_c) = Y_0 + \left[\frac{1 - Y_0}{A} e^{-B_1 \eta_c} - Y_0 \right] (1 - e^{-B_2 \eta_c}) \quad (27)$$

where $Y_0 = \frac{f_c^0}{f_c^{\text{fiber}}}$ (f_c^0 is the initial yield stress of SFRC; f_c^{fiber} is the uniaxial compressive strength of SFRC) and $\eta_c = \frac{\epsilon_{\text{inc}}}{\epsilon_{\text{inc}}^p}$ (ϵ_{inc} is the inelastic compressive strain of SFRC as described in Figure 2 and ϵ_{inc}^p is the inelastic compressive strain at the peak stress). The constants must follow

Equations (28) and (29) to ensure that the peak occurs at $Y = 1$:

$$B_1 = \frac{B_2 e^{-B_2}}{1 - e^{-B_2}} \frac{1 - Y_0}{1 - Y_0 e^{-B_2}} \quad (28)$$

$$A = e^{-B_1} (1 - e^{-B_2}) \frac{1 - Y_0}{1 - Y_0 e^{-B_2}} \quad (29)$$

The slope of the postpeak response of the stress–strain curve is governed by parameter B_2 as expressed in Equation (30). As aforementioned, the postpeak slope of the uniaxial compressive behavior in the case of SFRC decreases with the increase of the fiber volume fraction. To consider this phenomenon, the following nonlinear relationship between B_2 and the volume fractions of fibers V_f is adopted as follows¹⁷:

$$B_2 = 0.1 - 0.08 (12.5 \times V_f)^{0.1} \quad (30)$$

Furthermore, the compressive strength of SFRC, f_c^{fiber} , and the strain at the peak stress ϵ_c^p were demonstrated to be a function of the fiber volume fraction (V_f) and aspect ratio ($a_f = \frac{L_f}{d_f}$).^{43,44} The variation of f_c^{fiber} and ϵ_c^p with the volume fraction and aspect ratio of fiber are expressed by the following equations:

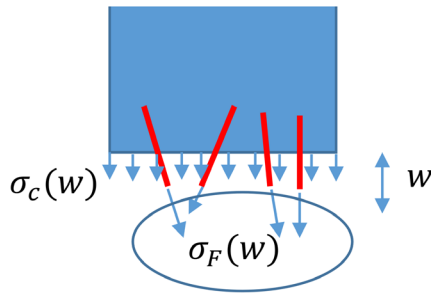
$$f_c^{\text{fiber}}(V_f, a_f) = f_c' (1 + \lambda_v(V_f) \cdot \lambda_a(a_f)) \quad (31)$$

$$\epsilon_c^p(V_f, a_f) = \epsilon_{c0}^p (1 + \lambda_{ve}(V_f) \cdot \lambda_{ae}(a_f)) \quad (32)$$

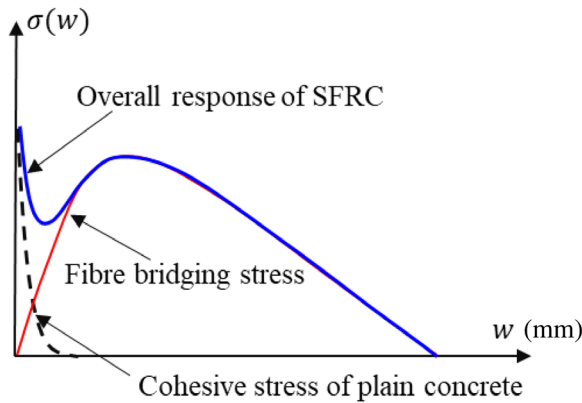
where f_c' and ϵ_{c0}^p are, respectively, the compressive strength and strain at the peak stress of plain concrete. Four parameters λ_v , λ_a , λ_{ve} , and λ_{ae} are expressed by the Equations (A8)–(A11) in Appendix A.

3.4.2 | Tensile behavior

The mechanisms governing the behavior of plain concrete and SFRC can be identified via typical experimental results of tension tests, shown in Figure 3. In the case of plain concrete, a single major crack forms immediately after the stress exceeding the tensile strength of concrete matrix, and quickly dissipating all the energy, leading to a very sharp decrease in the postpeak behavior. In contrast, a considerable enhancement in the toughness and fracture resistance can be observed from the behavior of SFRC. This is due to the bridging effect of fibers during the opening process of the first crack, which enables to transfer further stresses between two sides of the crack.



(a) Force diagram at the crack surface of SFRC



(b) Stress vs crack opening relationship of SFRC

FIGURE 9 Conceptual model of steel fiber reinforced concrete (SFRC). (a) Force diagram at the crack surface of SFRC. (b) Stress versus crack opening relationship of SFRC.

The concept of uniaxial tension model of SFRC is illustrated in Figure 9. As can be seen from the figure, the tensile force transferring at an opening crack include two parts: (1) the concrete cohesive resistance ($\sigma_c(w)$) and (2) the fiber bridging stress ($\sigma_F(w)$). Therefore, the overall response of SFRC can be expressed in the following equation:

$$\sigma_{\text{FRC}}(w) = \sigma_c(w) + \sigma_F(w) \quad (33)$$

where σ_{FRC} is the overall tension stress of SFRC and w is the crack opening displacement.

The following subsections present the procedure to simulate the postcracking response of SFRC. Section 3 exhibits the cohesive stress of plain concrete while the full bridging stress of fibers at crack surface can be obtained by following the procedures in Sections 3.4.2.2, 3.4.2.3, and 3.4.2.4. Section 3.4.2.5 introduces the method to combine the cohesive stress of plain concrete and fiber bridging stress to obtain the overall tension stress response of SFRC.

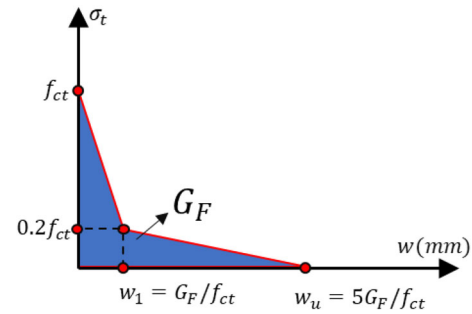


FIGURE 10 Bilinear cohesive crack model of plain concrete (stress vs. crack opening displacement).

Cohesive stress of plain concrete $\sigma_c(w)$

Using cohesive crack models is the simplest method to describe the fracture process of concrete material. In those models, it is assumed that a cohesive crack is a fictitious crack able to transfer stress from one side to the another. As a result, the tension softening behavior of concrete can be fully described by the relationship between cohesive stress and crack opening. According to previous studies in the literature, the bilinear function of the stress-crack opening law is one of the simplest, yet reliable, model to capture the softening response of concrete material.^{45,46} The bilinear model adopted in this study is illustrated in Figure 10, which is governed by two parameters including the tensile strength of plain concrete (f_{ct}) and fracture energy (G_F). Those two parameters f_{ct} and G_F can be obtained by using the equations suggested by FIB model⁴⁷ and Equations (A3) and (A4) in Appendix A presented by Bažant and Becq-Giraudon.⁴² The relationship of stress (σ_c) and crack opening displacement w in the bilinear model can be expressed as follows:

$$\sigma_c = \begin{cases} f_{ct} - 0.8f_{ct} \frac{w}{w_1} & w < w_1 = \frac{G_F}{f_{ct}} \\ 0.2f_{ct} - 0.2f_{ct} \frac{w - w_1}{w_u - w_1} & w_1 < w < w_u = \frac{5G_F}{f_{ct}} \\ 0 & w_u < w \end{cases} \quad (34)$$

Crack bridging stress $\sigma_F(w)$ due to fiber pull out mechanism

The fiber bridging law can be obtained by integrating the individual contribution of all fibers across the crack surface as illustrated in Figure 11. Due to the random distribution, the probability density functions of the orientation of fibers $p(\theta)$ and the distance between the crack surface and fiber centroid $p(z)$ are necessary to be incorporated in the integration. According to Lin and

Li,⁴⁸ the model of fiber bridging cracks can be expressed in the following equation:

$$\sigma_F(w) = \frac{4V_f}{\pi(d_f)^2} \int_{\theta=0}^{\pi/2} \int_{z=0}^{(l/2)\cos\theta} P(w, \theta, z) p(\theta) p(z) dz d\theta \quad (35)$$

where $P(w, \theta, z)$ is the pull-out force of a single fiber at a crack surface. In the case of uniform random distribution ($p(\theta) = \sin\theta$ and $p(z) = \frac{2}{L_f}$), Equation (35) can be rewritten as:

$$\sigma_F(w) = \frac{8V_f}{\pi L_f (d_f)^2} \int_{\theta=0}^{\pi/2} \int_{z=0}^{(l/2)\cos\theta} P(w, \theta, z) \sin\theta dz d\theta \quad (36)$$

However, the feasibility of analytical derivation of Equation (36) relies on the complexity of pull-out function $P(w, \theta, z)$. To ensure the generality of the model, the numerical form of Equation (36) according to Gauss-Legendre quadrature rule⁴⁹ is expressed as follows:

$$\sigma_F(w) = \frac{8V_f}{\pi L_f (d_f)^2} \sum_{i=1}^{10} \sum_{j=1}^{10} P(w, \theta_i, z_j) \sin\theta_i \psi(\theta_i) \psi(z_j) \quad (37)$$

where $\theta_i, z_j, \psi(\theta_i)$, and $\psi(z_j)$ are determined from the Legendre polynomial (as described in Appendix C).

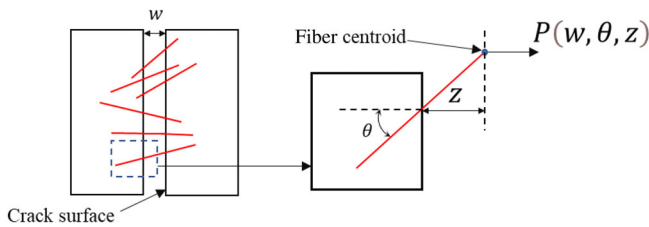


FIGURE 11 Illustration of fiber bridging.

The detail for calculating the numerical integration can be found in Appendix A. The fiber bridging model can be fully obtained when the pull-out response of a single fiber at the crack surface is determined. The pull-out function of straight fibers and hook-end fibers are presented in the below sections.

Pull out behavior of straight steel fiber

This section presents the derivation of the relationship between pull-out force and crack opening displacement of straight steel fibers. In this study, it is assumed that fibers are pulled out from the side associated with the shorter embedded length.⁴⁸ The pull-out response of a fiber includes two phases: (a) debonding phase and (b) pull-out phase (see Figure 12). The interfacial frictional slip between a fiber and matrix is activated when the debonding of the fiber occurs. During the debonding phase, the interface of matrix and the fiber is divided into two zones consisting of the intact zone and the debonded zone with length l as described in the figure. The length of debonded zone increases with the applying pull-out force P . When l reaches the embedded length of the fiber L , the fiber is debonded completely from the matrix, which means the fiber is completely pulled out from the matrix. During the pull-out phase without rupture, the total rigid-body movement of the fiber is considerably larger than elastic deformation of the fiber.^{48,50} According to the schematic diagram of fiber pull-out response described in Figure 12, the interfacial slip Δ between fiber and matrix can be calculated from the following differential equation proposed by Bao and Song⁵⁰:

$$\frac{d^2 \Delta}{dx^2} = \frac{4(1+\eta)}{E_f d_f} \tau(\Delta) \quad (38)$$

where τ is the interfacial stress between fiber and matrix, E_f and d_f are, respectively, the elastic modulus and diameter of the fiber, and constant η is determined by Equation (39)

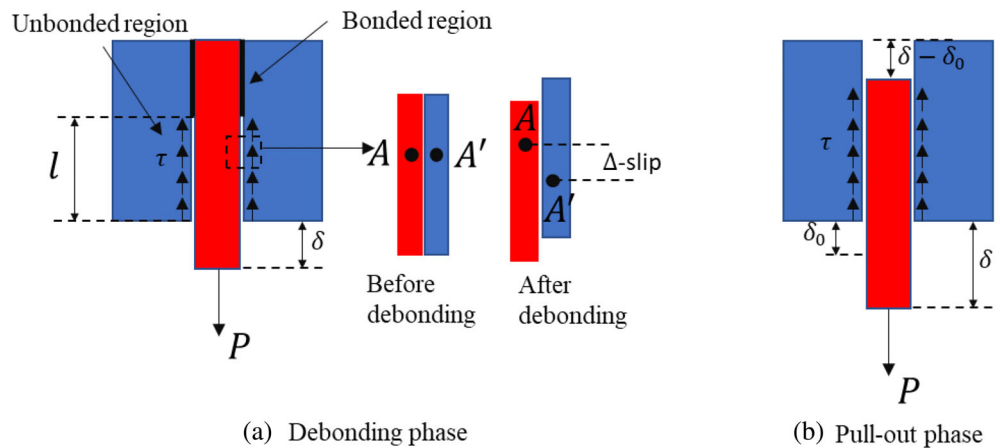


FIGURE 12 Schematic diagram of the pull-out response of a single fiber.

$$\eta = \frac{V_f E_f}{(1 - V_f) E_c} \quad (39)$$

where V_f is the volume fraction of fiber. To solve Equation (38), the constitutive relation between the interfacial stress $\tau(\Delta)$ and the slip Δ is required. According to Le et al.,¹⁹ a linear softening relationship should be adopted for straight steel fibers, and the model is expressed as follows:

$$\tau(\Delta) = \tau_0 \left(1 - \beta \frac{\Delta}{d_f} \right) \quad (40)$$

where τ_0 is the frictional sliding shear stress at the tip of debonding zone where no slip occurs ($\Delta = 0$), β is a non-dimensional softening parameter, and d_f is the fiber diameter. However, the experimental findings of the pull-out response of steel fibers and concrete matrix demonstrated an exponential shape instead of linear function.⁵¹ Therefore, this study adopted the exponential slip-softening function proposed by Bao and Song⁵⁰ for the interfacial relationship of steel fiber and concrete matrix. The function is presented as follows:

$$\tau(\Delta) = \tau_0 e^{\left(-\beta \frac{\Delta}{d_f} \right)} \quad (41)$$

From this relationship, the pull-out model for a straight steel fiber perpendicular to the crack surface with the crack opening displacement w is expressed as follows:

$$P = \frac{\sqrt{2} \pi d_f^2 \tau_0 (1 + \eta)}{\omega} \sqrt{1 - \frac{1}{\exp\left(\frac{\beta w}{2d_f}\right)}} \quad \text{for } 0 \leq w \leq w_0 \quad (42)$$

for the debonding phase, and

$$P = \frac{\sqrt{2} \pi d_f^2 \tau_0 (1 + \eta)}{\omega} \exp\left(\frac{-\beta(w - w_0)}{d_f}\right) \times \left(\tanh h \frac{\omega L}{\sqrt{2} d_f} - \tanh h \frac{\omega(w - w_0)}{\sqrt{2} d_f} \right) \quad (43)$$

for the fiber pull-out phase ($w_0 \leq w \leq L + w_0$), where

$$\eta = \frac{V_f E_f}{(1 - V_f) E_m}$$

$$\omega = \sqrt{4(1 + \eta)\beta\tau_0/E_f}$$

$$w_0 = \frac{4d_f}{\beta} \ln \left(\cosh \frac{\omega L}{\sqrt{2} d_f} \right) \quad (44)$$

and $P = 0$ when $w \geq L + w_0$. V_f , E_f , E_m , and L are the volume fractions of fibers, elastic modulus of fiber, elastic modulus of concrete matrix, and embedded length of fiber in concrete matrix, respectively; and w_0 is the crack opening displacement at the instant when the debonding along full length of the embedded fiber segment completes.

Equations (42) and (43) are applicable to fibers perpendicular to the crack surface. For nonperpendicular fibers with an inclined angle θ as described in Figure 12, previous studies showed that such orientation significantly affects the pull-out force P . It is also found that due to the snubbing effect, P increases with the increase of the inclination angle from 0° to 30° .^{48,51} The snubbing factor α_{snub} can be calculated using the following equation:

$$\alpha_{\text{snub}} = e^{f\theta} \quad (45)$$

where f is the snubbing coefficient and taken as 0.9 for steel fiber.⁵² However, when the inclined angle θ is larger than 30° , the pull-out force decreased significantly due to the occurrence of matrix spalling phenomenon.⁵² The matrix spalling effect can be expressed as:

$$\alpha_{\text{spal}} = (\cos\theta)^k \quad (46)$$

where k is the spalling coefficient and taken as 1.6 for concrete matrix.^{52,53} Both snubbing and matrix spalling effect can be incorporated in the pull-out force equation as follows:

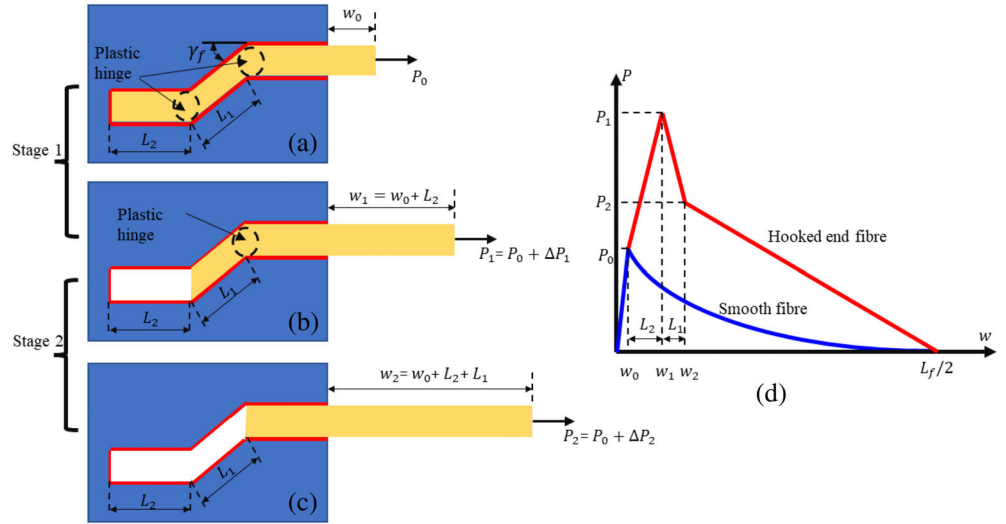
$$P(w, \theta, z) = P(w, \theta = 0, z) \alpha_{\text{snub}} \alpha_{\text{spal}} \quad (47)$$

where $P(w, \theta = 0, z)$ is calculated based on Equations (42) and (43).

Pull out behavior of hooked end fiber

Experimental findings indicated that hooked-end fibers exhibit a significantly higher pull-out strength and pull-out work owing to the anchorage effect of hook parts.^{54–56} This study adopts the concept of a frictional pulley along two plastic hinges to consider the mechanical anchorage of the hook into the pull-out model of hook-end fibers.^{55,56} The concept of the model is

FIGURE 13 (a) Complete debonding of hooked-end fiber; (b) complete straightening of the first part of the hook; (c) complete straightening of two parts of hook; and (d) simplified pull-out model of hooked-end fiber.



illustrated in Figure 13 at which the pull-out phase of hooked-end steel fibers undergoes the cold work deformation through the plastic hinge to straighten the hook. From the figure, the straightening process can be divided into 2 stages. In the first stage (see Figure 13a,b), both parts of fiber L_1 and L_2 are straightened at two plastic hinges and the corresponding increase of pull-out load ΔP_1 can be determined as follows^{55,56}:

$$\Delta P_1 = \frac{\sigma_y \pi d_f^2}{12 \cos \gamma_F (1 - \mu \sin \frac{\gamma_F}{2})^2} \quad (48)$$

where σ_y is the yield strength of fiber, μ is the kinetic friction coefficient of matrix and fiber and taken as 0.9, and γ_F is the hook angle as described in Figure 13. After stage 2, when the hook part L_2 is totally pulled out from the matrix, there is only one plastic hinge of hook part L_1 is active. Therefore, the pull-out load drops to P_2 with the corresponding increase ΔP_2 contributed by only one plastic hinge as follows^{55,56}:

$$\Delta P_2 = \frac{\sigma_y \pi d_f^2}{24 \cos \gamma_F (1 - \mu \sin \frac{\gamma_F}{2})} \quad (49)$$

With the contribution of mechanical anchorage presented above, the extended pull-out model for hooked-end fiber is described in Figure 13d. For the debonding phase with $0 \leq w \leq w_0$, the pull-out force is calculated similarly to the case of smooth fiber according to Equation (42). For the straightening contribution from both plastic hinges with $w_0 \leq w \leq w_0 + L_2$, the pull-out force is calculated as follows:

$$P = P_0 + \frac{\Delta P_1}{L_2} (w - w_0) \quad (50)$$

For the straightening contribution from one plastic hinge with $w_0 + L_2 \leq w \leq w_0 + L_2 + L_1$, the pull-out force is determined by using the following expression:

$$P = P_0 + \Delta P_1 + \frac{\Delta P_2 - \Delta P_1}{L_1} (w - w_0 - L_2) \quad (51)$$

After the straightening process, the fiber is subsequently pulled out of the matrix by the same frictional mechanism as experienced by a smooth fiber as described in the previous section. However, instead of adopting Equation (43) for $w_0 + L_2 + L_1 \leq w \leq w_0 + L$, the pull-out force is now simplified by a linear approximation as follows:

$$P = \frac{P_0 + \Delta P_2}{L_1 + L_2 - L} (w - w_0 - L) \quad (52)$$

P_0 is the pull-out force at the moment when the complete debonding along the full length of the embedded part of fiber occurs, and calculated based on Equation (42) as follows:

$$P_0 = \frac{\sqrt{2} \pi d_f^2 \tau_0 (1 + \eta)}{\omega} \sqrt{1 - \frac{1}{\exp\left(\frac{\beta w_0}{2 d_f}\right)}} \quad \text{for } 0 \leq w \leq w_0 \quad (53)$$

Cohesive model for overall tensile response of SFRC

From Equations (42)–(53), the entire response of the pull-out behavior of smooth or hooked-end fibers can be obtained. By substituting those responses into numerical integration as presented in Equation (37), the fiber bridging stress response for SFRC is determined. The detailed example for calculating the model step-by-step is

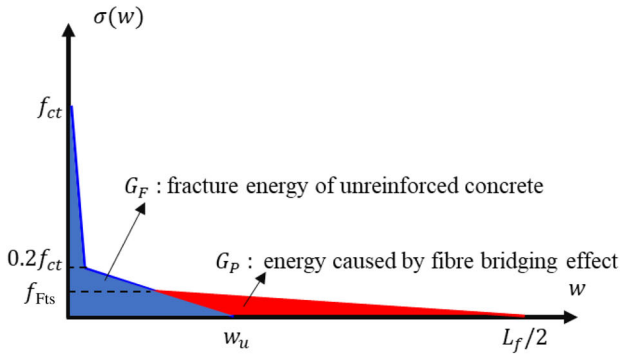
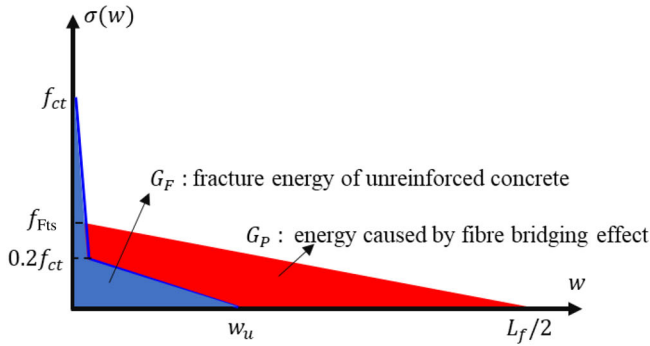
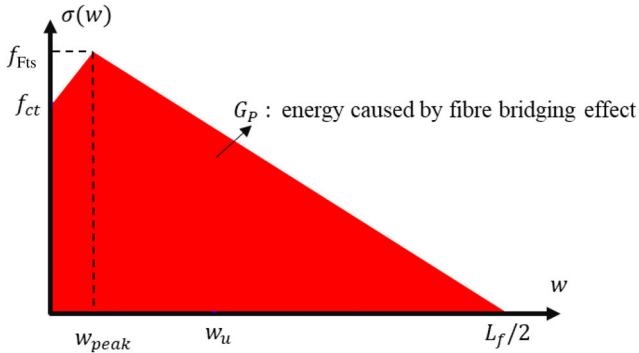
(a) Softening behaviour when $f_{Fts} < 0.2f_{ct}$ (b) Softening behaviour when $f_{ct} > f_{Fts} > 0.2f_{ct}$ (c) Hardening behaviour when $f_{Fts} > f_{ct}$

FIGURE 14 The simplified concept for steel fiber reinforced concrete model. (a) Softening behavior when $f_{Fts} < 0.2f_{ct}$. (b) Softening behavior when $f_{ct} > f_{Fts} > 0.2f_{ct}$. (c) Hardening behavior when $f_{Fts} > f_{ct}$.

presented in Appendix A. The overall tensile response of SFRC can be obtained by summing the cohesive stress of plain concrete and fiber bridging stress as expressed in Equation (34). However, this procedure leads to complicated stress–strain curves of SFRC, which is not favorable for being adopted in the numerical simulation. In this study, the trilinear and bilinear curves described in

Figure 14 are adopted as those curves were demonstrated to be simple but effective to model the overall tensile response of both plain concrete and SFRC.^{45,57} To capture the physical phenomenon of the fiber bridging at crack, the proposed models illustrated in Figure 14 must include two parts, where the blue part represents the contribution of fracture energy of plain concrete G_F and red part is the contribution of bridging energy G_p due to fibers at cracks. G_p can be calculated by integrating the Equation (37) as follows:

$$G_p = \int_{w=0}^{w=L_f/2} \sigma_F(w) dw \quad (54)$$

and the numerical form as:

$$G_p = \frac{8V_f}{\pi L_f (d_f)^2} \sum_{k=1}^{10} \sum_{i=1}^{10} \sum_{j=1}^{10} P(w_k, \theta_i, z_j) \sin \theta_i \psi(\theta_i) \psi(z_j) \psi(w_k) \quad (55)$$

In the proposed model, a fictitious tensile stress f_{Fts} is introduced to control the softening and hardening behaviors of SFRC, and determined from G_p by the following equation:

$$f_{Fts} = \frac{2G_p}{\frac{L_f}{2} - w_u} \quad (56)$$

where w_u is the ultimate crack opening displacement of plain concrete as mentioned in the previous section. If $f_{Fts} < 0.2f_{ct}$, the model adopts the trilinear function as described in Figure 14a. The analytical form of the cohesive cracking stress of SFRC is expressed as follows:

$$\sigma_{FRC}(w) = \begin{cases} f_{ct} - 0.8f_{ct} \frac{w}{w_1} & w < w_1 = \frac{G_F}{f_{ct}} \\ \frac{0.2f_{ct}w_u - f_{Fts}w_1}{w_{Fts} - w_1} - \frac{(0.2f_{ct} - f_{Fts})w}{w_{Fts} - w_1} & w_1 < w < w_{Fts} \\ \frac{f_{Fts}L_f}{L_f - 2w_{Fts}} - \frac{2f_{Fts}w}{L_f - 2w_{Fts}} & \frac{L_f}{2} > w > w_{Fts} \\ 0 & w > \frac{L_f}{2} \end{cases} \quad (57)$$

where w_{Fts} is the corresponding displacement at fictitious tensile stress f_{Fts} and calculated by

$$w_{Fts} = w_u - \frac{f_{Fts}(w_u - w_1)}{0.2f_{ct}} \quad (58)$$

In the case of f_{Fts} calculated from Equation (56), which is larger than $0.2f_{ct}$ but still smaller than f_{ct} , the model will follow the bilinear function as illustrated in

Figure 14b, and then f_{Fts} and w_{Fts} are recalculated to ensure that the area of red part shown in Figure 14b equal to the bridging energy G_p :

$$f_{Fts} = \frac{G_p + \frac{3}{8}G_F}{\frac{L_f}{4} - \frac{w_1}{1.6}} \quad (59)$$

$$w_{Fts} = \frac{(f_{ct} - f_{Fts})w_1}{0.8f_{ct}} \quad (60)$$

Subsequently, the cohesive crack stress model of FRC described in Figure 14b is determined as follows:

$$\sigma_{FRC}(w) = \begin{cases} f_{ct} - (f_{ct} - f_{Fts})\frac{w}{w_{Fts}} & w < w_{Fts} \\ \frac{f_{Fts}L_f}{L_f - 2w_{Fts}} - \frac{2f_{Fts}w}{L_f - 2w_{Fts}} & w_{Fts} < w < \frac{L_f}{2} \\ 0 & w > \frac{L_f}{2} \end{cases} \quad (61)$$

In the case of f_{Fts} calculated from Equation (56) which is larger than f_{ct} , the cohesive cracking stress of FRC undergoes the hardening behavior as described as Figure 14c. As the contribution of fracture energy of plain concrete is negligible in the case of hardening behavior, the area under stress-crack opening relationship can be assumed equaling to the bridging energy due to fibers at cracks G_p . Then the peak stress f_{Fts} of model is recalculated as follows:

$$f_{Fts} = \frac{4G_p - 2w_{peak}f_{ct}}{L_f} \quad (62)$$

where w_{peak} is assumed to be equivalent to the crack opening displacement at peak stress of fiber bridging contribution. In other words, w_{peak} is extracted during the calculation process of fiber bridging stress $\sigma_F(w)$ by Equation (37). Then the analytical formula for hardening behavior is presented as follows:

$$\sigma_{FRC}(w) = \begin{cases} f_{ct} + (f_{Fts} - f_{Fts})\frac{w}{w_{peak}} & w < w_{peak} \\ f_{Fts} - f_{Fts}\frac{w - w_{peak}}{\frac{L_f}{2} - w_{peak}} & w_{peak} < w < \frac{L_f}{2} \\ 0 & w > \frac{L_f}{2} \end{cases} \quad (63)$$

From Equations (56)–(63), the total response of stress-crack opening displacement under uniaxial

conditions of SFRC can be determined. In general, the proposed model is simple but effective to capture the fiber bridging effect through three key parameters including G_p , f_{Fts} , and w_{peak} . Those parameters are determined based on the procedures of Sections 3.4.2.2, 3.4.2.3, and 3.4.2.4 and presented in Appendix A.

3.5 | Damage evolution

The determination of damage variables in this study is based on the definition of the compressive and tensile variables as the portion of normalized energy dissipated by damage^{23,58}:

$$d_c = \frac{1}{g_c} \int_0^{\varepsilon_{inc}} \sigma_c(\varepsilon_{inc}) d\varepsilon_{inc}; d_t = \frac{1}{g_t} \int_0^{\varepsilon_{int}} \sigma_t(\varepsilon_{int}) d\varepsilon_{int} \quad (64)$$

where ε_{inc} and ε_{int} are inelastic compressive (crushing) and tensile (cracking) strain, respectively; and g_c and g_t are, respectively, the total energies per unit volume dissipated through the entire deterioration process of compression and tension:

$$g_c = \int_0^{\infty} \sigma_c(\varepsilon_{inc}) d\varepsilon_{inc}; g_t = \int_0^{\varepsilon_{int}^u} \sigma_t(\varepsilon_{int}) d\varepsilon_{int} \quad (65)$$

By substituting the compressive hardening rule in Equation (27) into Equations (64) and (65), the normalized crushing energy and compressive damage variable of SFRC can be determined in Equations (A12) and (A13) of Appendix A.

For the tension behavior, the cracking strain is determined from the crack opening displacement w based on the crack band theory. The fundamental feature of the crack band theory is that the given constitutive relation with cracking strain must be associated with a certain width l_{eq} of the crack band (as illustrated in Figure 15)⁵⁹:

$$\varepsilon_{inc} = \frac{w}{l_{eq}} \quad (66)$$

where l_{eq} is a material constant representing the crack band width. By substituting Equation (66) into the integrations of Equations (64) and (65), the tension damage variable can be calculated as:

$$g_t = \frac{G_F + G_p}{l_{eq}} \quad (67)$$

$$d_t = \frac{1}{G_F + G_p} \int_0^w \sigma_t(w) dw \quad (68)$$

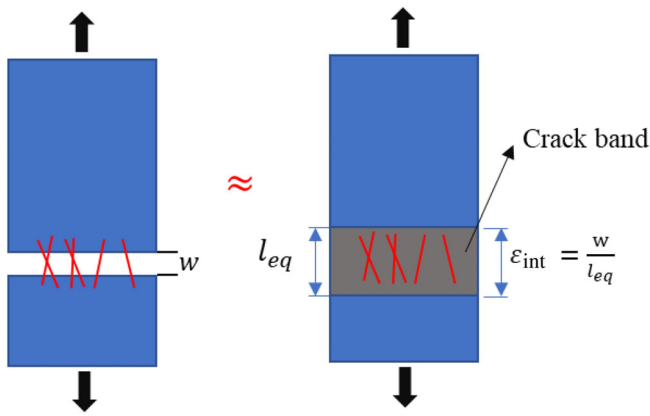


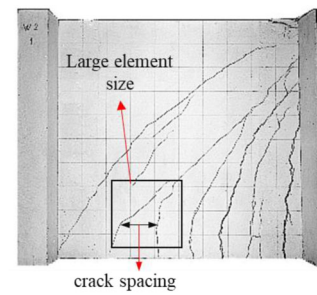
FIGURE 15 Illustration of crack band theory.

where G_F is the fracture energy of plain concrete, G_p is the energy caused by bridging effect of fibers, and $\sigma_t(w)$ is the total tension stress of FRC $\sigma_{FRC}(w)$, which is determined by the equations presented in Section 3.4.2.5. Then, through the substitution of Equations (56)–(63) into Equation (68), the analytical formulas of tension damage variable can be obtained and presented in Appendix B.

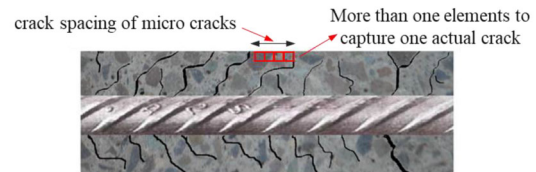
In numerical simulation, l_{eq} is normally taken as the length of the smallest element.^{46,58} This ensures that only a single crack band or crack occurs in each finite element.⁶⁰ However, if l_{eq} is selected based on element size, this will lead to the inaccuracy in predicting the post-crack behavior of concrete in the following two cases:

1. Element size is larger than the realistic maximum crack spacing.
2. Element size is smaller than the realistic minimum crack spacing.

In the first situation, there might be more than one actual crack localizing inside each finite element as seen from Figure 16a. This means that the large element size can result in the underestimation of energy dissipation during postcrack stage. Meanwhile, the very fine element size can lead to the prediction of higher number of cracks in an actual crack band as shown in Figure 16b. Hence, the energy dissipated during postcrack stage is overestimated and the stiffer response compared to actual behavior is obtained. Based on those reasons, two limits on the band width are introduced as follows $L_{min} \leq l_{eq} \leq L_{max}$, where L_{min} and L_{max} are the minimum and maximum crack spacing, respectively. The minimal limit L_{min} can be related to the internal structures of the material and recommended from a_g to $3a_g$, where a_g is the maximum aggregate size. In practice, L_{min} ranges from 10 to 50 mm. The maximum limit L_{max} should correspond to the



(a) Element size larger than the maximum crack spacing (image adopted from [61])



(b) Element size smaller than the minimum crack spacing (image adopted from [61])

FIGURE 16 Two problems when using inappropriate element size (a) Element size larger than the maximum crack spacing (image adopted from Červenka et al.⁶¹) (b) Element size smaller than the minimum crack spacing (image adopted from Červenka et al.⁶¹).

typical crack spacing of concrete structures adopting reinforcing bars. It can be estimated from spacing of reinforcing bars in each structural element. In general, if the element size is in the range between L_{min} and L_{max} , l_{eq} corresponds to the element size. In other cases, l_{eq} equals L_{max} for coarse elements and L_{min} for fine elements.

4 | NUMERICAL VERIFICATION


The steps of deriving the corresponding SFRC material parameters based on the fiber and concrete material properties and fiber configurations are given in Appendices. After the completion of model derivations, it is significant to verify the proposed model against experimental data in terms of both the material and structural scales. In this section, the reliability of the model is validated by comparing the numerical results with experimental data from material and structural tests. The above derivation is adopted to modify the CDPM in Abaqus.

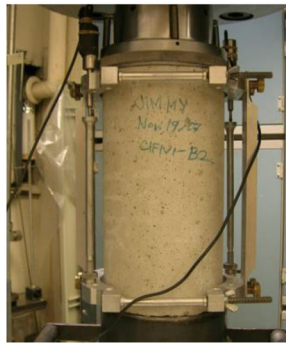
4.1 | Verification with material tests

4.1.1 | Uniaxial compressive tests

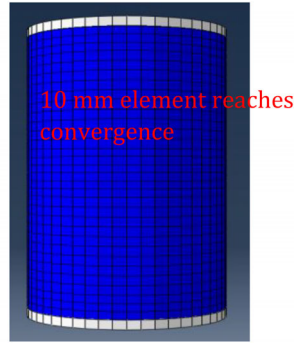
The experimental results of the uniaxial compressive test from the previous study are selected for verification.⁶²

TABLE 1 Material properties of fibers for compressive tests.⁶²

| | L_f (mm) | d_f (mm) | E_f (GPa) |
|---|------------|------------|-------------|
|  | 50 | 0.62 | 210 |



(a) Test setup



(b) Numerical model

FIGURE 17 Numerical models and experimental setup of uniaxial compressive tests. (a) Test setup. (b) Numerical model.

The compressive strength of plain concrete matrix was 49 MPa. The properties of hooked end steel fiber are presented in Table 1. The height and diameter of cylinder specimens were, respectively, 300 and 150 mm, and the test setup is illustrated in Figure 17a.

For the numerical model by using Abaqus, a three-dimensional eight-node linear brick solid element (C3D8R) with integration reduction is adopted to simulate the cylindrical specimens as describe in Figure 17b. The displacement-controlled loads are employed in the model as per the experiment. The model converged at element size of 10 mm after carrying out a convergence test, therefore, it is adopted for modeling all cases.

The numerical results are verified with the test data and plotted in Figure 18. It can be seen that the stress-strain curves of numerical models agree well with those obtained from experiment in all cases with different volume fractions of fiber. This indicates that the modified model can capture the effect of volume fraction on post-peak behavior of SFRC under uniaxial compression.

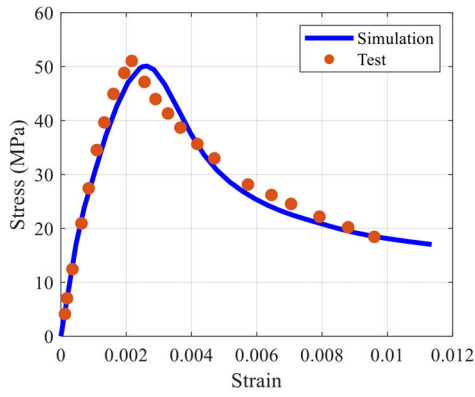
4.1.2 | Uniaxial tension tests

Uniaxial tension tests (Figure 19a) from another study are adopted to verify the capability of the proposed model for capturing the tension behavior of SFRC. The experiment was conducted by Amin et al.⁶³ with two types of commercially available steel fibers including hooked-end (HE) Dramix[®] RC-65/35-BN cold-drawn wire fibers and

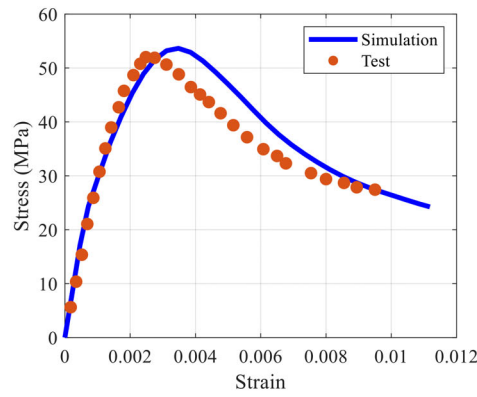
OL13/0.20 straight (S) high carbon steel fibers. The compressive strength of the concrete matrix was 60 MPa and the properties of fibers are summarized in Table 2. The maximum size of aggregate a_g was 10 mm, thus the minimum limit for crack band width L_{\min} is taken as a_g . For validation purpose of material tests, since the element is normally meshed finely, the maximum limit is not necessary to be considered.

To reduce the simulation time, the uniaxial tension tests are simulated in 2D plane stress condition using a mesh comprising 2028 three-node triangular elements as shown in Figure 18b. The previous studies indicated that using 2D plane stress can reliably simulate the uniaxial response.^{17,19} The size of element in the middle of specimen is 5 mm which is smaller than L_{\min} . Therefore, the crack bandwidth l_{eq} must equal L_{\min} . The comparison of numerical results and experimental data is illustrated in Figure 20. Three parameters τ_0 , β , and σ_y to determine the pull-out behavior of straight and hooked-end steel fiber are calibrated based on the test data of specimen reinforced with 0.5% volume fraction of fibers (as shown in Figure 20a,c). Subsequently, those calibrated parameters are used for the case of 1% volume fraction of fibers. The results from Figure 20 show a fair correlation between numerical findings and test data for different types of fibers with volume fractions ranging from 0 to 1%. This indicates that the three parameters τ_0 , β , and σ_y calibrated in the case of 0.5% fiber volume fraction can be used to simulate softening-behavior of SFRC with higher fiber volume fraction up to 1%. In future, if more data are available, recalibration for a similar fiber volume fraction should be carried out.

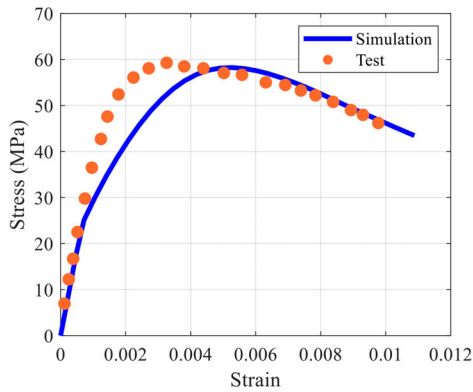
Meanwhile, the incorporation of high-volume fraction of fibers may lead to the strain-hardening response of SFRC. To evaluate the capability of the proposed model for capturing the strain-hardening response, the results from uniaxial tensile tests conducted by are used for verification. The test setup is illustrated in Figure 21a while the numerical model is presented in Figure 21b. The properties of fibers are tabulated in Table 3. The calibration for three parameters τ_0 , β , and σ_y is conducted based on the test data of specimen reinforced with 2% volume fraction. The calibrated values of those parameters are summarized in Table 2. The comparison between the numerical results and experimental data is plotted in



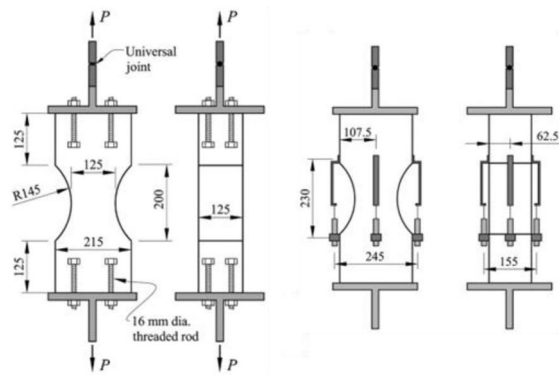
(a) $V_f = 0.5\%$



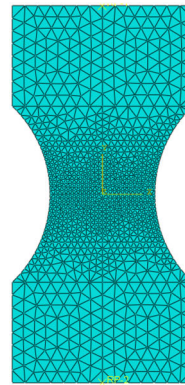
(b) $V_f = 1\%$



(c) $V_f = 1.5\%$



(a) Details of tensile specimens and test setup



(b) Numerical model of tensile specimens

FIGURE 18 Verification with test results (compression behavior) obtained from Susetyo.⁶² (a) $V_f = 0.5\%$, (b) $V_f = 1\%$, and (c) $V_f = 1.5\%$.

FIGURE 19 Numerical models and test setup of uniaxial tensile tests conducted by Amin et al.⁶³ (a) Details of tensile specimens and test setup. (b) Numerical model of tensile specimens.

Figure 22. It can be seen that the stress–strain curves obtained from the finite element model give a fair agreement with the test data. When the volume fraction of fibers is lower than 3%, the model can capture well the behavior of SFRC. With higher volume fraction up to 6%, the peak stress of the curve still can be successfully predicted by the proposed model while the ascending branch

of the curve is not well simulated. This discrepancy in the tension stiffness as shown in Figure 22 can be attributed to the simplification of the strain-hardening behavior of SFRC under tension as mentioned in Section 3.4.2.5. The bilinear function as described in Figure 14c might not be appropriate to capture accurately the shape of strain hardening stress–strain curve of

TABLE 2 The properties of Dramix® RC-65/35-BN and OL13/0.20.⁶³

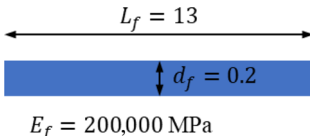
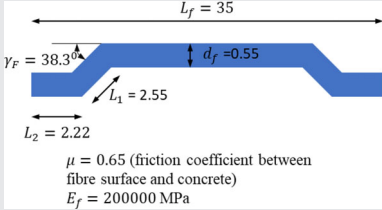
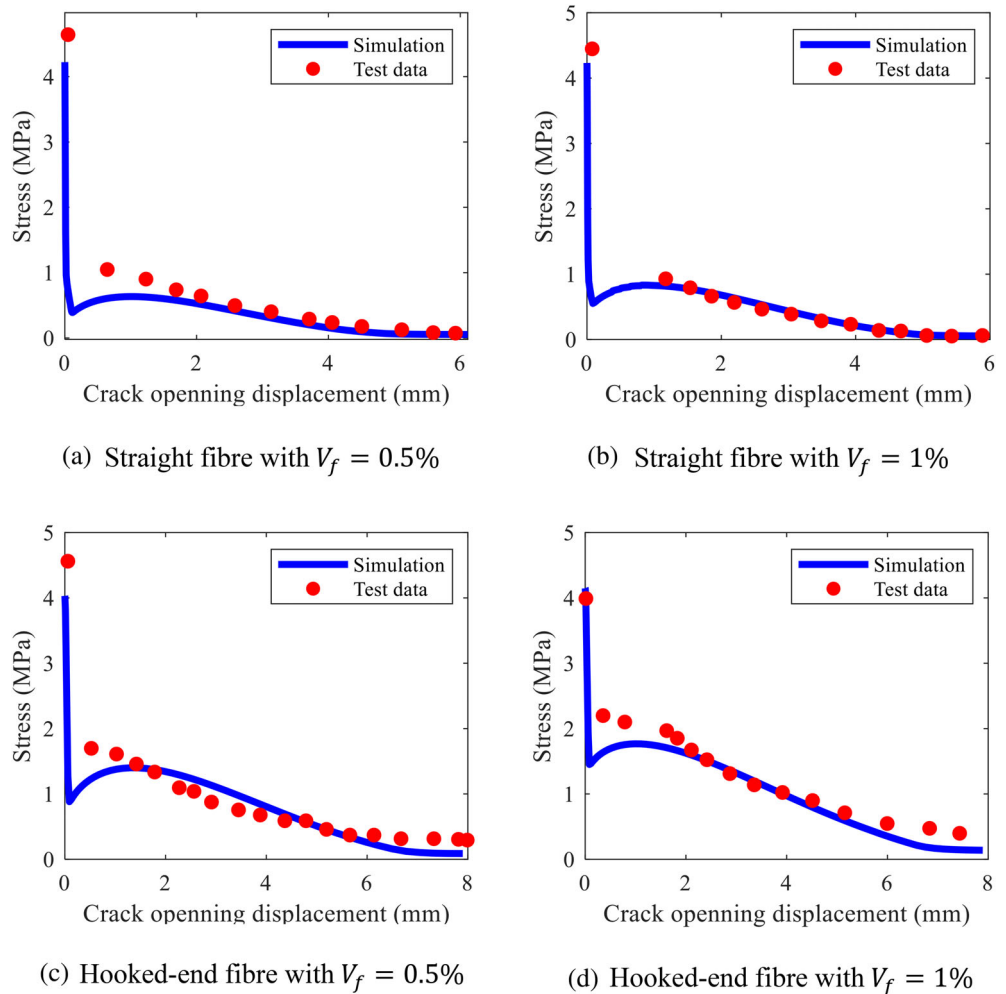
| Labels | Fiber configuration | τ_0 (MPa) | β | σ_y (MPa) |
|-------------|--|----------------|---------|------------------|
| OL13/0.20 |  <p>$L_f = 13$ $d_f = 0.2$ $E_f = 200,000$ MPa</p> | 1.6 | 0.01 | NA |
| RC-65/35-BN |  <p>$L_f = 35$ $d_f = 0.55$ $\gamma_f = 38.3^\circ$ $L_1 = 2.55$ $L_2 = 2.22$ $\mu = 0.65$ (friction coefficient between fiber surface and concrete) $E_f = 200000$ MPa</p> | 1.6 | 0.01 | 600 |

FIGURE 20 Verification with test results (direct tension with low fiber volume fraction) obtained from Amin et al.⁶³
 (a) Straight fiber with $V_f = 0.5\%$.
 (b) Straight fiber with $V_f = 1\%$.
 (c) Hooked-end fiber with $V_f = 0.5\%$.
 (d) Hooked-end fiber with $V_f = 1\%$.



SFRC. Further studies can be conducted in future to improve the model with higher fiber volume fraction.

4.2 | Verification with structural tests

To further verify the proposed model in a large scale with a complex stress state, the experimental data of large-

scaled fiber reinforced concrete beams with T section from the previous study⁶⁵ is adopted. The details of beam dimension and reinforcing rebars are presented in Figure 23. Hooked-end steel fibers with 0.75 mm in diameter and 60 mm in length were used in that study. The details of fiber geometry are presented in Table 4. The specified yield strength of longitudinal and transverse reinforcing steel bars was 500 MPa. The cylinder

compressive strength of concrete without fiber reinforcement was 23.6 MPa. Further details for test setup can be found in the reference.⁶⁵

The numerical model adopts the truss elements (T3D2) and solid elements (C3D8R) to model reinforcing bars and concrete beams, respectively. The interaction between rebars and concrete is modeled by the Embedded Region Constraint function. The elasto-plastic material model is adopted to model the steel bars. A mesh size convergence test is carried out, and finally, the most appropriate mesh size for the whole model is selected at 10 mm (see Figure 24). Three parameters τ_0 , β , and σ_y are calibrated based on the test data of specimen reinforced with 0.75% volume fraction. Those calibrated values are adopted in the numerical simulation of specimens reinforced with 1% fiber volume fraction.

The comparison between the numerical results and test data is plotted in Figure 25. The initial stiffness of beams from the numerical models is higher than that of tested beams. The similar phenomenon was reported

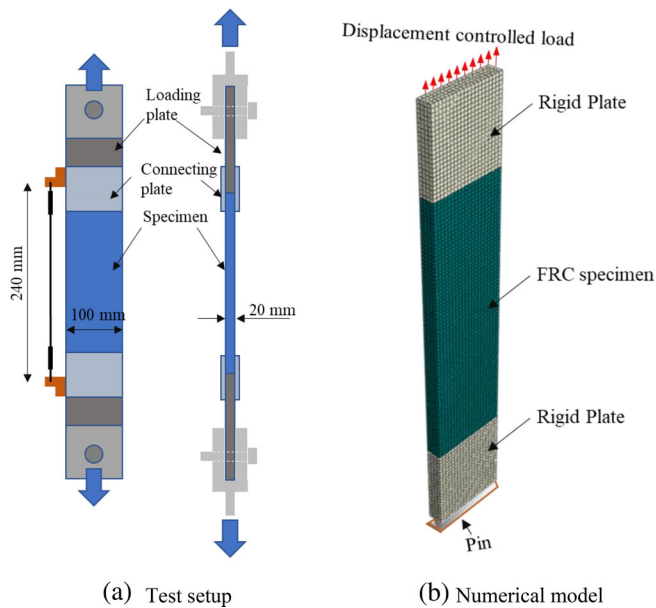


FIGURE 21 The uniaxial tests conducted by Zongjin et al.⁶⁴ and numerical model proposed in this study. (a) Test setup and (b) numerical model.

in the previous study.^{66,67} The main cause of the phenomenon might be attributed to the fact that the actual elastic modulus of concrete from the tests might be smaller than that determined by the empirical Equation (A2). Furthermore, the imperfections in the boundary condition of test setup of experiment such as inaccuracy of alignment or poor contact of supports and specimen can lead to the low stiffness behavior at the beginning of the test.⁶⁷ Due to the assumption of ideal conditions of test setup, the numerical models might not reflect the actual initial stiffness of the tested beams. However, in terms of the load-carrying capacity, the proposed model can yield a good prediction and capture the effect of fiber on the beam capacity.

The failure mode of test specimens and damage contour of the beams is visualized in Figure 26. It can be seen that the beam without fiber reinforcement fails by diagonal tension failure with the formation of a single inclined crack (see Figure 26a). The tension damage contour of numerical beam without fiber shows the agreement with crack profile captured from the tests. Meanwhile, the results of beam with 1% of fiber reinforcement indicate the uniform distribution of tension damage through the shear span of the beam. This can be

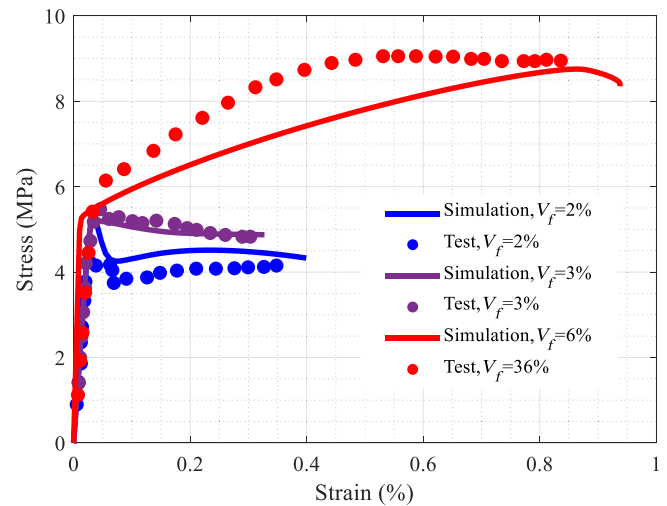


FIGURE 22 Verification with the test results (direct tension with high fiber volume fraction) obtained from Zongjin et al.⁶⁴

| Labels | Fiber configuration | τ_0 (MPa) | β | σ_y (MPa) |
|----------|--|----------------|---------|------------------|
| Dramix 1 | <p>$\mu = 0.65$ (friction coefficient between fibre surface and concrete) $E_f = 200000$ MPa</p> | 1.4 | 0.01 | 700 |

TABLE 3 The properties of Dramix fiber used in previous study.⁶⁴

FIGURE 23 The configuration of T-beam and reinforcement details.⁶⁵

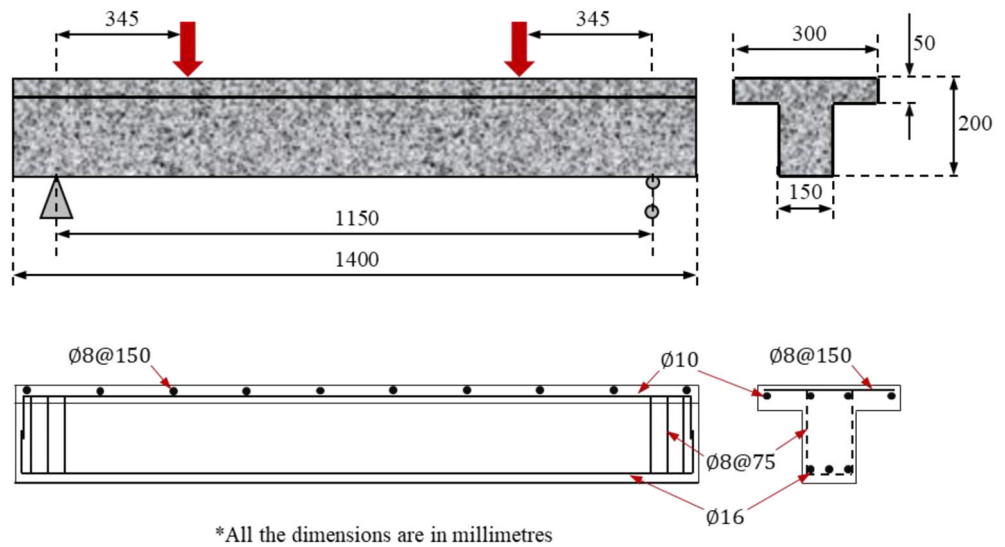
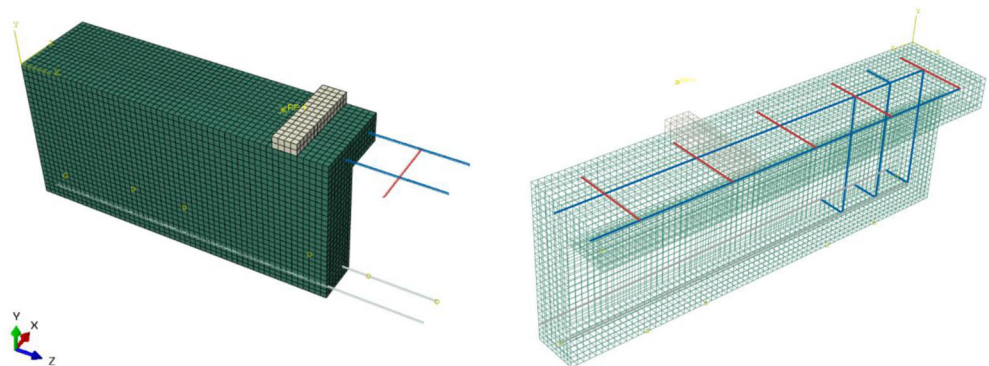


TABLE 4 The properties of hooked end steel fiber.⁶⁵

| Labels | Fiber configuration | τ_0 (MPa) | β | σ_y (MPa) |
|----------|--|----------------|---------|------------------|
| Dramix 1 | <p>$\mu = 0.65$ (friction coefficient between fibre surface and concrete) $E_f = 200000$ MPa</p> | 0.97 | 0.01 | 900 |

FIGURE 24 3D FEM model of the T-beams.



explained that due to bridging effect of fibers, the opening of the first tensile crack is postponed, and thus more diagonal cracks are formed. Therefore, the tension damage can be transferred through multiple cracks instead of a single critical crack. The crack profile of the tested beam demonstrated the numerous inclined cracks formed in the shear span, which can be equivalent to the uniform damage from the simulation. It is noted that the proposed model could not visualize the formation of discontinuous cracks because the continuum damage mechanics theory is adopted for capturing the stress-strain response of element.⁶⁸ This issue was also reported in previous studies where the cracks could not be

visualized.^{17,58} However, the model is still able to reflect reasonably the stress transferring response of SFRC beams. At failure, the beam reinforced with fiber fails by combining shear and compressive flexural mode as described in Figure 26b. The model is also able to capture the compressive damage due to the bending response (see Figure 26b).

5 | CONCLUSION

A new approach to modify CDPM for simulating SFRC structures is proposed in this study. Although the

approach is derived for capturing the effect of steel fibers, it is a generic procedure and can be adopted for different types of fibers. The most significant contribution of this work is to analytically incorporate the bridging effect of fibers in SFRC.

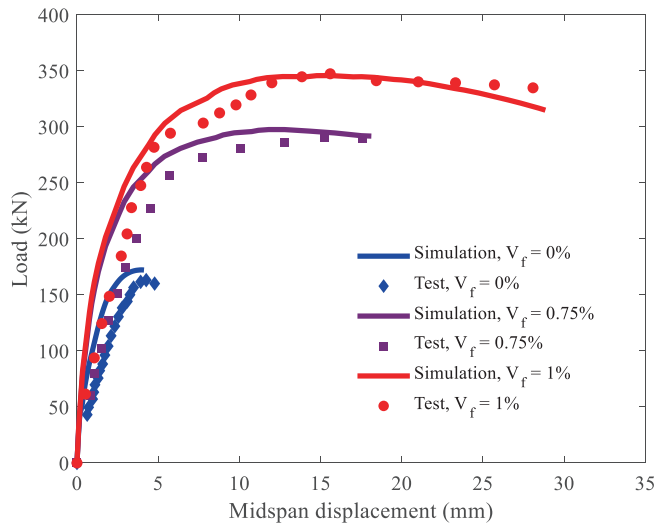


FIGURE 25 Verification of the proposed model with experimental beam test from Sahoo et al.⁶⁵

In terms of the yield function and plastic flow rule, the confining effect of fiber is integrated into the ratio of biaxial and uniaxial strength and the dilation angle.

For the compressive hardening/softening rules, empirical equations from the previous study are adopted to model the improvement in ductility, toughness, compressive strength, and strain at the peak load due to fiber reinforcement. Meanwhile, the bridging mechanism of fiber is incorporated in the tension softening curve of SFRC. The bridging mechanism is derived based on the integration of entire pull-out contribution of individual fiber at crack surfaces. The main parameters of the model including τ_0 , β , and σ_y are calibrated from material tests. According to the calibration, it can be recommended that β is not sensitive in all cases and can be taken as 0.01, yield strength of fiber σ_y ranges from 600 to 900 MPa, and τ_0 is related to the compressive strength f'_c in the following relationship $0.2\sqrt{f'_c}$. By adopting the recommended parameter in the modified model, the response of SFRC with the variation of fiber volume fraction (up to 6%) and geometry can be simulated without conducting further material tests.

The damage evolution laws are derived based the portion of normalized energy dissipated by damage.^{13,42} Through the verification with experimental data, the proposed model demonstrates its capability to simulate the

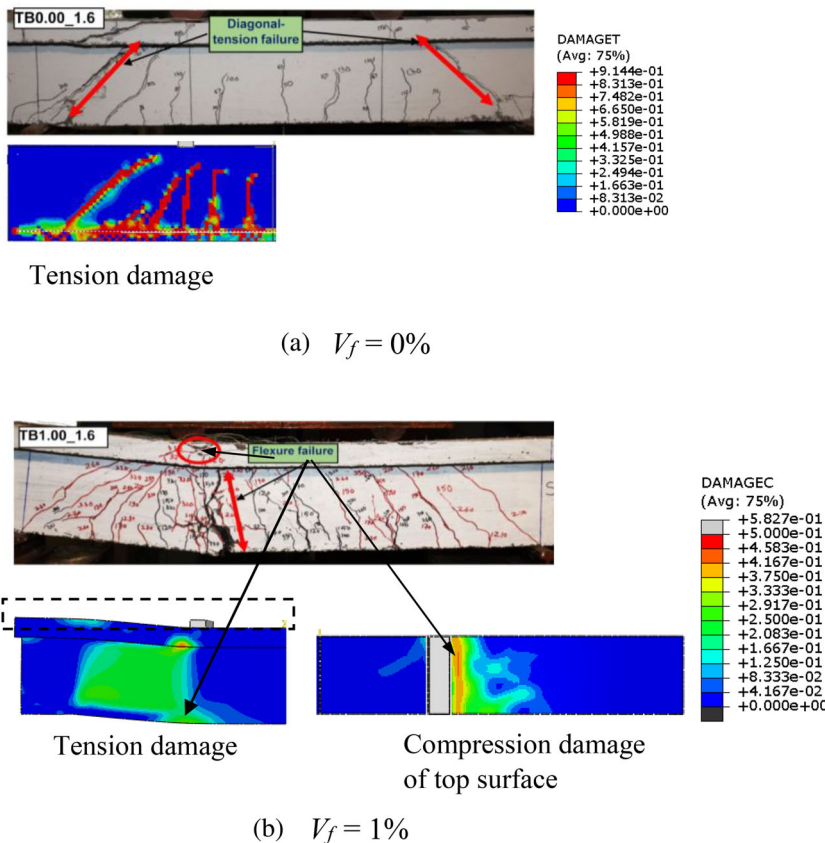


FIGURE 26 Crack profile of the tested beams⁶⁹ and damage contour of simulated beams (a) $V_f = 0\%$ and (b) $V_f = 1\%$.

effect of fiber parameters on the response of SFRC structures.

NOTATION

| | |
|---------------------------------------|---|
| α | parameter in yield function governing the biaxial compressive stress state |
| β | nondimensional softening parameter in slip model |
| γ | parameter in yield function governing the triaxial compressive stress state |
| γ_F | Hook angle |
| $\bar{\epsilon}_{pc}$ | equivalent compressive plastic strain |
| $\bar{\epsilon}_{pt}$ | equivalent tension plastic strain |
| ϵ_c^p | strain at the peak stress of SFRC |
| ϵ_{c0}^p | strain at the peak stress of plain concrete |
| θ | fiber orientation |
| μ | friction coefficient of matrix and fiber |
| $\bar{\sigma}_c(\bar{\epsilon}_{pc})$ | effective compressive cohesion stress |
| $\bar{\sigma}_t(\bar{\epsilon}_{pt})$ | effective tension cohesion stress |
| $\bar{\sigma}_{max}$ | maximum of principal stress |
| $\sigma_{FRC}(w)$ | overall tension stress of SFRC |
| $\sigma_c(w)$ | plain concrete cohesive stress |
| $\sigma_f(w)$ | fiber bridging stress |
| σ_{tu} | residual postcracking tensile stress |
| σ_{fu} | ultimate strength of fiber |
| σ_y | yield stress of steel fiber |
| τ_0 | frictional sliding shear stress at the tip of debonding zone |
| τ_u | ultimate bond strength between fiber and concrete matrix |
| ψ | dilation angle of plain concrete |
| ψ^F | dilation angle of SFRC |
| d_c | compressive damage variable |
| d_t | tension damage variable |
| d_f | fiber diameter |
| E_c | elastic modulus of plain concrete |
| E_f | elastic modulus of fiber |
| E_{FRC} | elastic modulus of SFRC |
| f | snubbing coefficient |
| f_{bc} | equibiaxial compressive strength of plain concrete |
| f_{bc}^{fiber} | equibiaxial compressive strength of SFRC |
| f_c^{fiber} | uniaxial compressive strength of SFRC |
| f_c' | uniaxial compressive strength of plain concrete |
| f_c^0 | initial yield stress of SFRC |
| f_{ct} | uniaxial tensile stress |
| f_{Fts} | fictitious tensile stress of SFRC |
| G_F | fracture energy of plain concrete |
| G_p | total bridging energy of fibers |
| k | spalling coefficient |
| L_f | fiber length |
| L_c | critical length of fiber |

| | |
|-------------------|--|
| l_{eq} | crack band width |
| K_c | ratio of second invariant on tensile meridian and compressive meridian |
| q | mises equivalent effective stress |
| p | effective hydrostatic pressure |
| $P(w, \theta, z)$ | pull-out force of a single fiber at a crack surface |
| V_f | volume fraction of fibers |
| w | crack opening displacement |
| w_u | ultimate crack opening displacement of plain concrete |
| z | distance between the crack surface and fiber centroid |

ACKNOWLEDGMENTS

This study deeply appreciates the support from the Australian Research Council Laureate Fellowships FL180100196. Open access publishing facilitated by University of South Australia, as part of the Wiley - University of South Australia agreement via the Council of Australian University Librarians.

DATA AVAILABILITY STATEMENT

The data that support the findings of this study are available from the corresponding author upon reasonable request.

ORCID

Thong M. Pham  <https://orcid.org/0000-0003-4901-7113>

Duong T. Tran  <https://orcid.org/0000-0001-7624-5977>

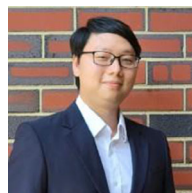
REFERENCES

1. Khan MZN, Hao Y, Hao H, Shaikh FUA. Mechanical properties of ambient cured high strength hybrid steel and synthetic fibers reinforced geopolymer composites. *Cem Concr Compos.* 2018;85:133–52.
2. Khan MZN, Hao Y, Hao H, Shaikh FUA. Experimental evaluation of quasi-static and dynamic compressive properties of ambient-cured high-strength plain and fiber reinforced geopolymer composites. *Construct Build Mater.* 2018;166:482–99.
3. Shi F, Pham TM, Hao H, Hao Y. Post-cracking behaviour of basalt and macro polypropylene hybrid fibre reinforced concrete with different compressive strengths. *Construct Build Mater.* 2020;262:120108.
4. Tran TT, Pham TM, Hao H. Experimental and analytical investigation on flexural behaviour of ambient cured geopolymer concrete beams reinforced with steel fibers. *Eng Struct.* 2019; 200:109707.
5. Tran TT, Pham TM, Hao H. Effect of hybrid fibers on shear behaviour of geopolymer concrete beams reinforced by basalt fiber reinforced polymer (BFRP) bars without stirrups. *Compos Struct.* 2020;243:112236.
6. Tran TT, Pham TM, Huang Z, Chen W, Hao H, Elchalakani M. Impact response of fibre reinforced geopolymer concrete beams with BFRP bars and stirrups. *Eng Struct.* 2021;231:111785.
7. Tran TT, Pham TM, Huang Z, Chen W, Ngo TT, Hao H, et al. Effect of fibre reinforcements on shear capacity of geopolymer

- concrete beams subjected to impact load. *Int J Impact Eng.* 2022;159:104056.
8. Ngo TT, Pham TM, Hao H. Effects of steel fibres and prestress levels on behaviour of newly proposed exterior dry joints using SFRC and CFRP bolts. *Eng Struct.* 2020;205:110083.
 9. Ngo TT, Pham TM, Hao H, Chen W, Elchalakani M. Performance of monolithic and dry joints with GFRP bolts reinforced with different fibres and GFRP bars under impact loading. *Eng Struct.* 2021;240:112341.
 10. Schaufert Edward A, Cusatis G. Lattice discrete particle model for fiber-reinforced concrete. I: theory. *J Eng Mech.* 2012;138:826–33.
 11. Schaufert Edward A, Cusatis G, Pelessone D, O'Daniel James L, Baylot JT. Lattice discrete particle model for fiber-reinforced concrete. II: tensile fracture and multiaxial loading behavior. *J Eng Mech.* 2012;138:834–41.
 12. Jin C, Buratti N, Stacchini M, Savoia M, Cusatis G. Lattice discrete particle modeling of fiber reinforced concrete: experiments and simulations. *Eur J Mech A/Solids.* 2016;57:85–107.
 13. Chi Y, Xu L, Mei G, Hu N, Su J. A unified failure envelope for hybrid fibre reinforced concrete subjected to true triaxial compression. *Compos Struct.* 2014;109:31–40.
 14. Chi Y, Xu L, Yu H-s. Constitutive modeling of steel-polypropylene hybrid fiber reinforced concrete using a non-associated plasticity and its numerical implementation. *Compos Struct.* 2014;111:497–509.
 15. Lee M, Kwak H-G, Park G-K. An improved calibration method of the K&C model for modeling steel-fiber reinforced concrete. *Compos Struct.* 2021;269:114010.
 16. Yang L, Lin X, Li H, Gravina RJ. A new constitutive model for steel fibre reinforced concrete subjected to dynamic loads. *Compos Struct.* 2019;221:110849.
 17. Mihai IC, Jefferson AD, Lyons P. A plastic-damage constitutive model for the finite element analysis of fibre reinforced concrete. *Eng Fract Mech.* 2016;159:35–62.
 18. Mihai IC, Jefferson AD. A micromechanics based constitutive model for fibre reinforced cementitious composites. *Int J Solids Struct.* 2017;110-111:152–69.
 19. Le LA, Nguyen GD, Bui HH, Sheikh AH, Kotousov A. Incorporation of micro-cracking and fibre bridging mechanisms in constitutive modelling of fibre reinforced concrete. *J Mech Phys Solids.* 2019;133:103732.
 20. Ngo TT, Pham TM, Hao H, Chen W, Ha NS. Proposed new dry and hybrid concrete joints with GFRP bolts and GFRP reinforcement under cyclic loading: testing and analysis. *J Build Eng.* 2022;49:104033.
 21. Madkour H, Maher M, Ali O. Finite element analysis for interior slab-column connections reinforced with GFRP bars using damage plasticity model. *J Build Eng.* 2022;48:104013.
 22. Le Minh H, Khatir S, Abdel Wahab M, Cuong-Le T. A concrete damage plasticity model for predicting the effects of compressive high-strength concrete under static and dynamic loads. *J Build Eng.* 2021;44:103239.
 23. Lubliner J, Oliver J, Oller S, Oñate E. A plastic-damage model for concrete. *Int J Solids Struct.* 1989;25:299–326.
 24. Lee J, Fenves GL. Plastic-damage model for cyclic loading of concrete structures. *J Eng Mech.* 1998;124:892–900.
 25. Kosaka Y, Tanigawa Y, Hatanaka S. Lateral confining stresses due to steel fibres in concrete under compression. *Int J Cem Compos Lightweight Concr.* 1985;7:81–92.
 26. Yin WS, Su ECM, Mansur MA, Hsu TTC. Fiber-reinforced concrete under biaxial compression. *Eng Fract Mech.* 1990;35:261–8.
 27. Murugappan K, Paramasivam P, Tan KH. Failure envelope for steel fiber concrete under biaxial compression. *J Mater Civ Eng.* 1993;5:436–46.
 28. Seow Puay Eng C, Swaddiwudhipong S. Failure surface for concrete under multiaxial load—a unified approach. *J Mater Civ Eng.* 2005;17:219–28.
 29. Traina LA, Mansour SA. Biaxial strength and deformational behavior of plain and steel fiber concrete. *ACI Mater J.* 1991;88:354–62.
 30. Jenn-Chuan Chern H-JY, Hong GWC. Behavior of steel fiber reinforced concrete in multiaxial loading. *ACI Mater J.* 1992;89:89.
 31. Pantazopoulou SJ, Zanganeh M. Triaxial tests of fiber-reinforced concrete. *J Mater Civ Eng.* 2001;13:340–8.
 32. Lu X, Hsu C-TT. Behavior of high strength concrete with and without steel fiber reinforcement in triaxial compression. *Cem Concr Res.* 2006;36:1679–85.
 33. Chi Y, Xu L, Yu H-S. Plasticity model for hybrid fiber-reinforced concrete under true Triaxial compression. *J Eng Mech.* 2014;140:393–405.
 34. Lim TY, Paramasivam P, Lee SL. Analytical model for tensile behavior of steel-fiber concrete. *Mater J.* 1987;84:286–98.
 35. Golpasand GB, Farzam M, Shishvan SS. Behavior of recycled steel fiber reinforced concrete under uniaxial cyclic compression and biaxial tests. *Construct Build Mater.* 2020;263:120664.
 36. Bao J, Wang L, Zhang Q, Liang Y, Jiang P, Song Y. Combined effects of steel fiber and strain rate on the biaxial compressive behavior of concrete. *Construct Build Mater.* 2018;187:394–405.
 37. Papanikolaou VK, Kappos AJ. Confinement-sensitive plasticity constitutive model for concrete in triaxial compression. *Int J Solids Struct.* 2007;44:7021–48.
 38. Ali Khajeh S, Mario MA. Lateral strain model for concrete under compression (with Appendix). *ACI Struct J.* 2014;111:441–51.
 39. Mirmiran A, Shahawy M. Dilation characteristics of confined concrete. *Mech Cohes Frict Mater.* 1997;2:237–49.
 40. Rousakis TC, Karabinis AI, Kiousis PD. FRP-confined concrete members: axial compression experiments and plasticity modeling. *Eng Struct.* 2007;29:1343–53.
 41. Yu T, Teng JG, Wong YL, Dong SL. Finite element modeling of confined concrete-I: Drucker–Prager type plasticity model. *Eng Struct.* 2010;32:665–79.
 42. Chi Y, Yu M, Huang L, Xu L. Finite element modeling of steel-polypropylene hybrid fiber reinforced concrete using modified concrete damaged plasticity. *Eng Struct.* 2017;148:23–35.
 43. Nataraja MC, Dhang N, Gupta AP. Stress–strain curves for steel-fiber reinforced concrete under compression. *Cem Concr Compos.* 1999;21:383–90.
 44. Ou Y-C, Tsai M-S, Liu K-Y, Chang K-C. Compressive behavior of steel-fiber-reinforced concrete with a high reinforcing index. *J Mater Civ Eng.* 2012;24:207–15.

45. Hoover CG, Bažant ZP. Cohesive crack, size effect, crack band and work-of-fracture models compared to comprehensive concrete fracture tests. *Int J Fract*. 2014;187:133–43.
46. Genikomsou AS, Polak MA. Finite element analysis of punching shear of concrete slabs using damaged plasticity model in ABAQUS. *Eng Struct*. 2015;98:38–48.
47. Taerwe L, Matthys S. *Fib model code for concrete structures 2010*. Lausanne, Switzerland: Ernst & Sohn, Wiley; 2013.
48. Lin Z, Li VC. Crack bridging in fiber reinforced cementitious composites with slip-hardening interfaces. *J Mech Phys Solids*. 1997;45:763–87.
49. von Winckel G. Legendre-Gauss quadrature weights and nodes Available from: <https://www.mathworks.com/matlabcentral/fileexchange/4540-legendre-gauss-quadrature-weights-and-nodes>. Natick, MA: MATLAB Central File Exchange; 2022.
50. Bao G, Song Y. Crack bridging models for fiber composites with slip-dependent interfaces. *J Mech Phys Solids*. 1993;41:1425–44.
51. Soetens T, Van Gysel A, Matthys S, Taerwe L. A semi-analytical model to predict the pull-out behaviour of inclined hooked-end steel fibres. *Construct Build Mater*. 2013;43:253–65.
52. Lee Y, Kang S-T, Kim J-K. Pullout behavior of inclined steel fiber in an ultra-high strength cementitious matrix. *Construct Build Mater*. 2010;24:2030–41.
53. Huo L, Bi J, Zhao Y, Wang Z. Constitutive model of steel fiber reinforced concrete by coupling the fiber inclining and spacing effect. *Construct Build Mater*. 2021;280:122423.
54. Laranjeira F, Molins C, Aguado A. Predicting the pullout response of inclined hooked steel fibers. *Cem Concr Res*. 2010;40:1471–87.
55. Abdallah S, Fan M, Rees DWA. Analysis and modelling of mechanical anchorage of 4D/5D hooked end steel fibres. *Mater Des*. 2016;112:539–52.
56. Abdallah S, Fan M, Rees DWA. Predicting pull-out behaviour of 4D/5D hooked end fibres embedded in normal-high strength concrete. *Eng Struct*. 2018;172:967–80.
57. Park K, Paulino GH, Roesler J. Cohesive fracture model for functionally graded fiber reinforced concrete. *Cem Concr Res*. 2010;40:956–65.
58. Alfarah B, López-Almansa F, Oller S. New methodology for calculating damage variables evolution in plastic damage model for RC structures. *Eng Struct*. 2017;132:70–86.
59. Planas J, Guinea GV, Elices M. Generalized size effect equation for quasibrittle materials. *Fatigue & Fract Eng Mater & Struct*. 1997;20(5):671–87.
60. Bažant ZP, Oh BH. Crack band theory for fracture of concrete. *Matér Construct*. 1983;16:155–77.
61. Červenka J, Červenka V, Laserna S. On crack band model in finite element analysis of concrete fracture in engineering practice. *Eng Fract Mech*. 2018;197:27–47.
62. Susetyo J. *Fibre reinforcement for shrinkage crack control in prestressed, precast segmental bridges*. Ontario, Canada: University of Toronto; 2009.
63. Amin A, Foster SJ, Muttoni A. Derivation of the σ - w relationship for SFRC from prism bending tests. *Struct Concr*. 2015;16:93–105.
64. Zongjin L, Faming L, Paul TY, Yiu-Wing M. Uniaxial tensile behavior of concrete reinforced with randomly distributed short fibers. *ACI Mater J*. 1998;95:95.
65. Sahoo DR, Bhagat S, Reddy TC. Experimental study on shear-span to effective-depth ratio of steel fiber reinforced concrete T-beams. *Mater Struct*. 2015;49:3815–30.
66. Nguyen KT, Ahn N, Le TA, Lee K. Theoretical and experimental study on mechanical properties and flexural strength of fly ash-geopolymer concrete. *Construct Build Mater*. 2016;106:65–77.
67. Al-Sabah S, Laefer DF, Truong Hong L, Phuoc Huynh M, Le J-L, Martin T, et al. Introduction of the intermeshed steel connection—a new universal steel connection. *Buildings*. 2020;10:37.
68. Mazars J, Pijaudier-Cabot G. Continuum damage theory—application to concrete. *J Eng Mech*. 1989;115:345–65.
69. Conforti A, Minelli F, Tinini A, Plizzari GA. Influence of polypropylene fibre reinforcement and width-to-effective depth ratio in wide-shallow beams. *Eng Struct*. 2015;88:12–21.
70. Venkateshan SP, Swaminathan P. Chapter 9 - numerical integration. In: Venkateshan SP, Swaminathan P, editors. *Computational methods in engineering*. Boston: Academic Press; 2014. p. 317–73.

AUTHOR BIOGRAPHIES



Tung T. Tran, Arup Perth, Exchange Plaza, 14, 14/2 The Esplanade, Perth WA 6152, Australia. Email: tung.tran@arup.com



Thong M. Pham, UniSA STEM, University of South Australia, Mawson Lakes, SA, 5095, Australia. Email: thong.pham@unisa.edu.au



Duong T. Tran, Center for Infrastructural Monitoring and Protection, School of Civil and Mechanical Engineering, Curtin University, Kent Street, Bentley, WA 6102, Australia. Email: t.tran86@postgrad.curtin.edu.au



Ngoc San Ha, School of Engineering, RMIT University, 124 La Trobe St, Melbourne VIC 3000, Australia. Email: ngoc.san.ha@rmit.edu.au



Hong Hao, Guangdong Provincial Key Laboratory of Earthquake Engineering and Applied Technology, Earthquake Engineering Research and Test Center, Guangzhou University, China; and Center for Infrastructural Monitoring and Protection, School of Civil and Mechanical Engineering, Curtin University, Kent Street, Bentley, WA 6102, Australia. Email: hong.hao@curtin.edu.au

How to cite this article: Tran TT, Pham TM, Tran DT, Ha NS, Hao H. Modified plastic damage model for steel fiber reinforced concrete. *Structural Concrete*. 2024. <https://doi.org/10.1002/suco.202300640>

APPENDIX A

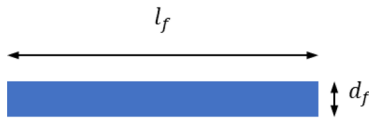
A.1 | Procedures for calculating parameters of the proposed CDPM-based model

- Step 1: Input the required material properties

A.1.1. | For fiber

Straight fiber

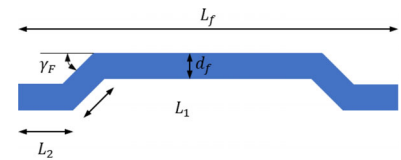
Straight fibre



E_f is elastic modulus of fibre
 V_f is volume fraction of fibre

Hooked-end fiber

Hooked-end fibre



$\mu = 0.65$ (friction coefficient between fibre surface and concrete)
 E_f is elastic modulus of fibre

A.1.2. | For concrete

f'_c (compressive strength of plain concrete in MPa), d_a (maximum aggregate size in mm), $\frac{w}{c}$ (water to cement ratio).

Strain at the peak stress of plain concrete⁴⁷

$$\varepsilon_{c0}^p = 0.003 \left(-0.4237 \left(\frac{f'_c}{120} \right)^2 + 0.8606 \left(\frac{f'_c}{120} \right) + 0.564 \right) \quad (\text{A1})$$

Elastic modulus for plain concrete⁴⁷

$$E_c = 21.5(10^3) \left(\frac{f'_c}{10} \right)^{1/3} \quad (\text{A2})$$

Tensile strength of plain concrete⁴⁷

$$f_{ct} = \begin{cases} 0.3(f'_c)^{2/3} & f'_c < 50 \text{ MPa} \\ 2.12 \ln(1 + 0.1(f'_c)) & f'_c \geq 50 \text{ MPa} \end{cases} \quad (\text{A3})$$

Fracture energy of plain concrete²⁹

$$G_F = 3.6 \left(\frac{f'_c}{0.051} \right)^{0.46} \left(1 + \frac{d_a}{11.27} \right)^{0.22} \left(\frac{w}{c} \right)^{-0.3} \quad (\text{A4})$$

Elastic modulus for SFRC

$$E_{\text{FRC}} = E_f V_f / 6 + E_c (1 - V_f / 6) \quad (\text{A5})$$

Compressive strength of SFRC

$$f_c^{\text{fiber}}(V_f, a_f) = f'_{c0} (1 + \lambda_v(V_f) \cdot \lambda_a(a_f)) \quad (\text{A6})$$

Strain at the peak stress of SFRC

$$\varepsilon_c^p(V_f, a_f) = \varepsilon_{c0}^p (1 + \lambda_{ve}(V_f) \cdot \lambda_{ae}(a_f)) \quad (\text{A7})$$

$$\lambda_v(V_f) = \frac{e^{125 \times V_f}}{15 + e^{125 \times V_f}} - 0.0625 \quad (\text{A8})$$

$$\lambda_a(a_f) = \left(\frac{a_f - 20}{80}\right)^{0.5} \quad (A9)$$

$$\lambda_{ve}(V_f) = 10 \times \left[\frac{e^{225 \times V_f}}{100 + e^{225 \times V_f}} - 0.0099 \right] \quad (A10)$$

$$\lambda_{ae}(a_f) = \left(\frac{a_f - 20}{80}\right)^3 \quad (A11)$$

A.1.3. | For the interface between concrete and fibers

The frictional sliding shear stress at the tip of debonding zone τ_0 and a nondimensional softening parameter β are determined based on the calibration of uniaxial tensile tests in Section 4.

- Step 2: Determine the parameters for the plasticity part of SFRC

+ Calculate the ratio $f_{bc}^{fiber}/f_c^{fiber}$ based on Equations (15) and (17).

+ Calculate dilation angle ψ^F based on Equations (17), (25), and (26).

- Step 3: Determine the compressive hardening/softening rules and compressive damage evolution

+ Adopt the values of f_c^{fiber} and ϵ_c^p determined in Step 1 to calculate the curve of stress versus inelastic compressive strain of SFRC based on Equations (27)–(30). The initial yield stress f_c^0 is taken as $0.6f_c^{fiber}$.

+ Calculate the normalized crushing energy of SFRC as follows

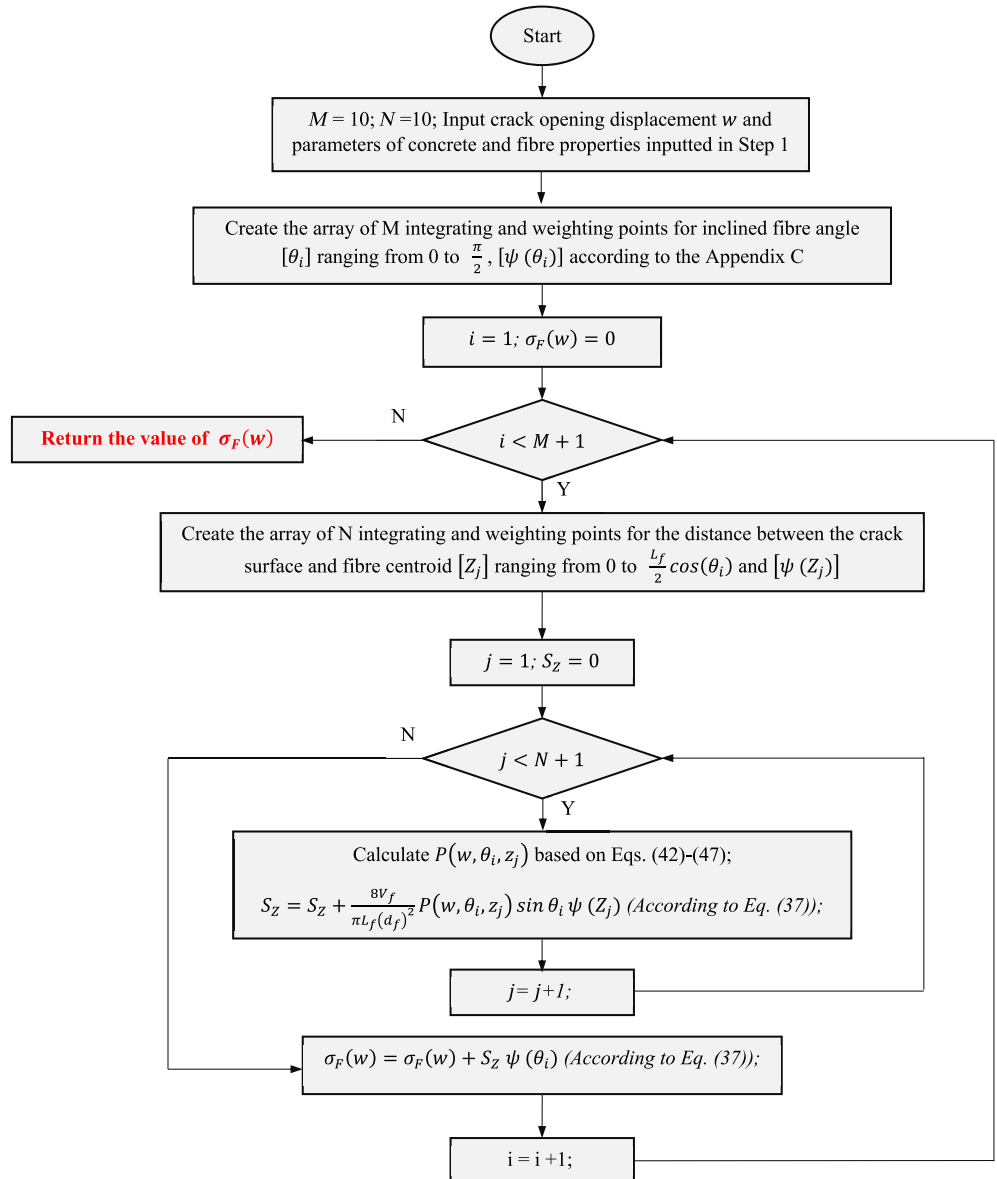


FIGURE A1 Flowchart A for calculating the bridging stress $\sigma_F(w)$.

FIGURE A2 Flowchart B for calculating the bridging energy G_p .

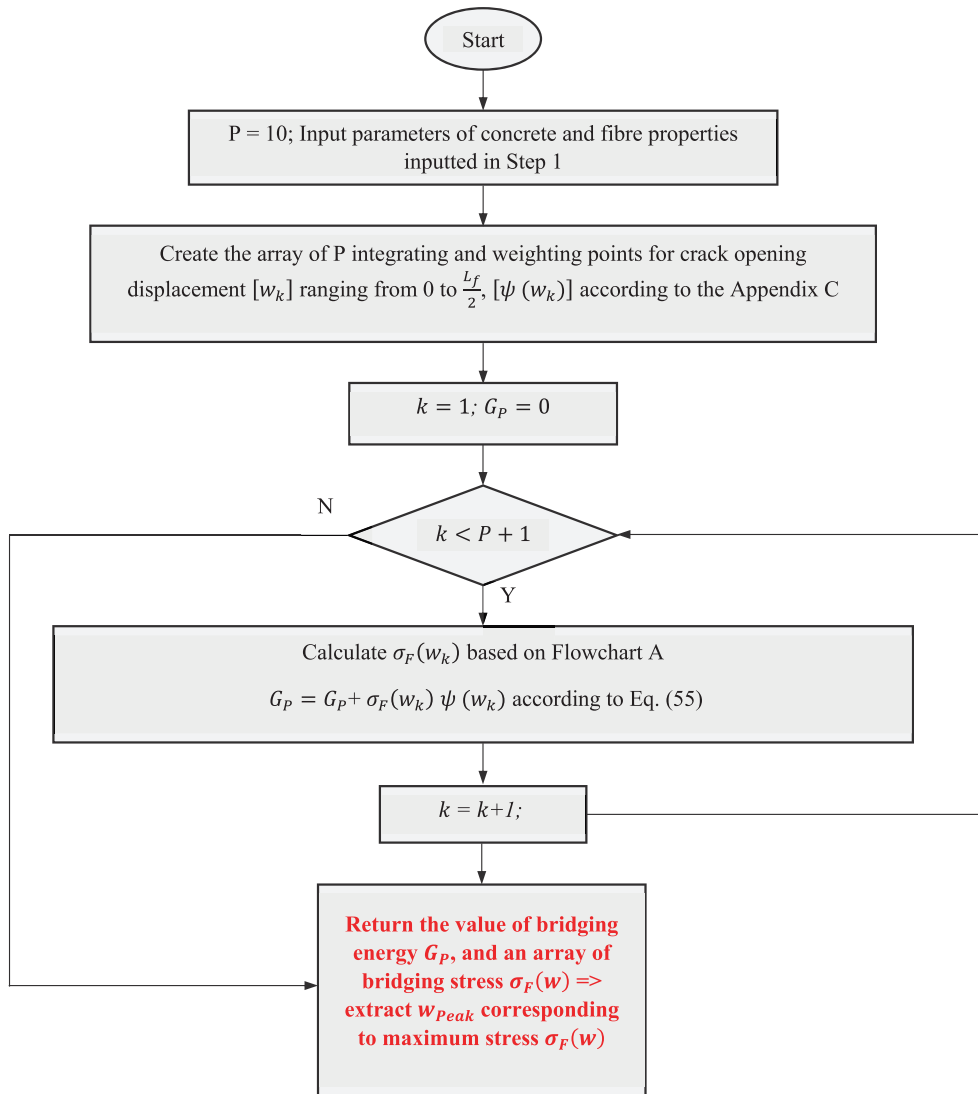
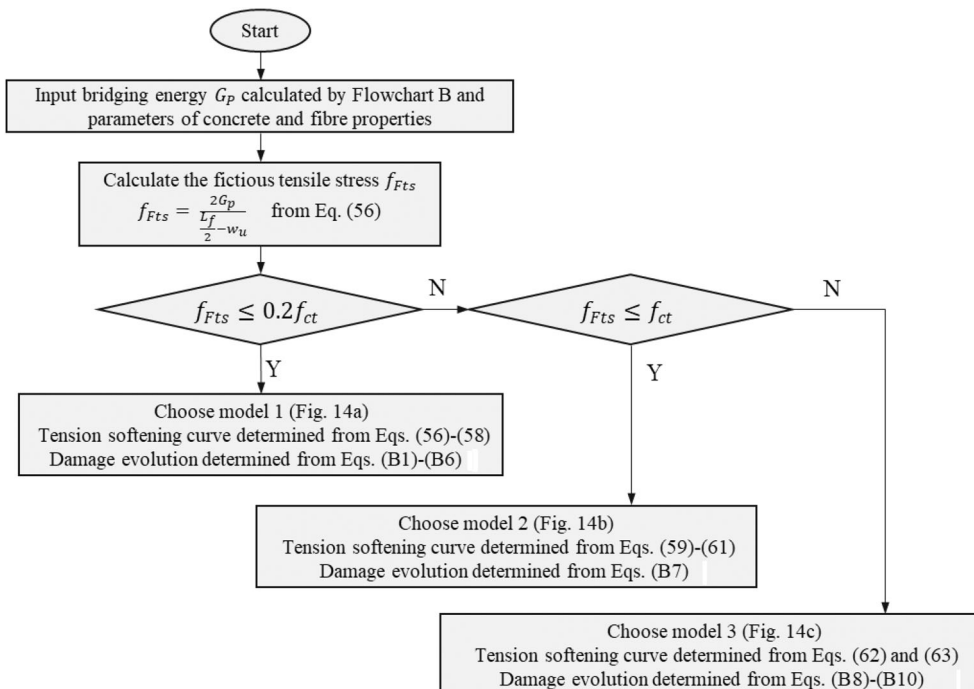


FIGURE A3 Flowchart C for determining the tension softening and damage curve of Steel fiber reinforced concrete.



$$g_c = \frac{Y_0}{B_2} + \frac{1-Y_0}{AB_1} - \frac{1-Y_0}{A(B_1+B_2)} \quad (\text{A12})$$

+ Subsequently, use g_c in Equation (64) to calculate the compressive damage variable of SFRC as follows

$$d_c = \frac{1}{g_c} \left(\frac{Y_0}{B_2} + \frac{1-Y_0}{AB_1} - \frac{1-Y_0}{A(B_1+B_2)} - \frac{Y_0 \exp(-B_2 X)}{B_2} - \frac{(1-Y_0) \exp(-B_1 X)}{(AB_1)} + \frac{(1-Y_0) \exp(-(B_1+B_2)X)}{A(B_1+B_2)} \right) \quad (\text{A13})$$

where $X = \frac{\epsilon_{inc}^D}{\epsilon_{inc}^P}$ (ϵ_{inc}^D is the inelastic compressive strain at the peak stress), and the constants A , B_1 , and B_2 determined in Equations (28)–(30)

- Step 4: Determine the tension softening rules and tension damage evolution of SFRC

+ Adopt the inputs in Step 1 for the calculation in flowcharts in Figures A1, A2, and A3

+ Calculate the bridging stress $\sigma_F(w)$ based on Flowchart A

+ Calculate the bridging energy G_p based on Flowchart B

+ Determine the tension softening and damage model of SFRC based on Flowchart C

$$d_t = \begin{cases} \frac{\left(f_{ct} w - 0.4 \frac{f_{ct} w^2}{w_1} \right)}{G_F + G_p} & w < w_1 = \frac{G_F}{f_{ct}} \\ \frac{D_1 w - D_2 w^2 - D_1 w_1 + D_2 w_1^2 + 0.6 f_{ct} w_1}{G_F + G_p} & w_1 < w < w_{Fts} \\ \frac{D_3 w - D_4 w^2 - D_3 w_{Fts} + D_4 w_{Fts}^2 + D_5}{G_F + G_p} & w_{Fts} < w < \frac{L_f}{2} \\ 1 & w = \frac{L_f}{2} \end{cases} \quad (\text{B1})$$

where

$$D_1 = \frac{0.2 f_{ct} w_{Fts} - f_{Fts} w_1}{w_{Fts} - w_1} \quad (\text{B2})$$

$$D_2 = 0.5 \frac{0.2 f_{ct} - f_{Fts}}{w_{Fts} - w_1} \quad (\text{B3})$$

$$D_3 = \frac{f_{Fts} L_f}{L_f - 2 w_{Fts}} \quad (\text{B4})$$

$$D_4 = \frac{f_{Fts}}{L_f - 2 w_{Fts}} \quad (\text{B5})$$

$$D_5 = 0.6 f_{ct} w_1 + 0.5 (w_{Fts} - w_1) (0.2 f_{ct} + f_{Fts}) \quad (\text{B6})$$

and f_{Fts} and w_{Fts} are, respectively, determined by Equations (56) and (58) in Section 3.4.2.5.

In the case of $f_{ct} > f_{Fts} > 0.2 f_{ct}$, the formula of tension damage variable is presented as:

$$d_t = \begin{cases} \left(\frac{f_{ct} w - 0.2 \frac{f_{ct} - f_{Fts}}{w_{Fts}} w^2}{G_F + G_p} \right) & w < w_{Fts} \\ \frac{D'_3 w - D'_4 w^2 - D'_3 w_{Fts} + D'_4 w_{Fts}^2 + 0.5 (f_{ct} + f_{Fts}) w_{Fts}}{G_F + G_p} & w_{Fts} < w < \frac{L_f}{2} \\ 1 & w = \frac{L_f}{2} \end{cases} \quad (\text{B7})$$

APPENDIX B

The damage evolution function of SFRC is derived by conducting the integration of Equations (67) and (68). If $f_{Fts} < 0.2 f_{ct}$, the tension damage variable is given as:

where the calculation of D'_3 and D'_4 is similar to that of D_3 and D_4 , in which the value of f_{Fts} and w_{Fts} is determined from Equations (59) and (60).

In the case of $f_{Fts} > f_{ct}$, the formula of tension damage variable is expressed as:

where

$$d_t = \begin{cases} \frac{\left(f_{ct}w + \frac{f_{Fts} - f_{ct}w^2}{2w_{peak}}\right)}{G_F + G_p} & w < w_{peak} \\ \frac{D_6w - D_7w^2 - D_6w_{peak} + D_7w_{peak}^2 + 0.5(f_{ct} + f_{Fts})w_{peak}}{G_F + G_p} & w_{peak} < w < \frac{L_f}{2} \\ 1 & w = \frac{L_f}{2} \end{cases} \quad (B8)$$

$$D_6 = \frac{f_{Fts}L_f}{L_f - 2w_{peak}} \quad (B9)$$

$$D_7 = \frac{f_{Fts}}{L_f - 2w_{peak}} \quad (B10)$$

and f_{Fts} and w_{peak} are determined by Equation (62) and Flowchart B, respectively.

APPENDIX C

The method to determine the integrating points and weights in Equations (37) and (55) including fiber orientation θ_i , distance z_i , and crack opening displacement w_i is presented in this Appendix.

The numerical integration of arbitrary function $f(x)$ with the range $[-1, 1]$ by using Gauss quadrature is expressed as follows⁷⁰:

$$I = \int_{-1}^1 f(x) dx = \sum_{i=1}^n \psi_i f(x_i) \quad (C1)$$

where n represents the number of Gauss points. Gauss quadrature integration yields exact values of integrals for polynomials of degree up to $2n - 1$. In this study, using 10 points is sufficient to obtain the accurate results. The Gauss points x_i is the i -th root of Legendre polynomial $P_n(x)$ determined as below:

$$P_n(x) = 2^n \sum_{k=0}^n \binom{n}{k} \binom{(n+k-2)/2}{k} x^k \quad (C2)$$

and the weights are given by the following formula:

TABLE C1 The Gauss points and weights with $n = 10$.

| x_i | ψ_i |
|--------------|----------|
| ± 0.1489 | 0.2955 |
| ± 0.4334 | 0.2693 |
| ± 0.6794 | 0.2191 |
| ± 0.8651 | 0.1495 |
| ± 0.9739 | 0.0667 |

$$\psi_i = \frac{2}{(1 - x_i^2) [P'_n(x_i)]^2} \quad (C3)$$

Based on MATLAB code,⁴⁹ the 10 Gauss points and weights are determined and presented in the Table C1.

If the limits of integration are arbitrary, for example, range of fiber orientation θ , distance z , or crack opening displacement w in Equations (37) and (55) is $[a, b]$, the integration points θ_i , z_i , w_i are determined by the following equation:

$$\theta_i \text{ or } z_i \text{ or } w_i = \frac{a+b}{2} + \frac{b-a}{2} x_i \quad (C5)$$

and the new weights ψ_i^{new} in range $[a, b]$ is calculated as follows:

$$\psi_i^{\text{new}} = \frac{b-a}{2} \psi_i \quad (C6)$$

By using Table C1 and Equations (C5) and (C6), θ_i , z_i , and w_i and weights can be determined.